AIChE WILEY InterScience DISCOVER SOMETHING GREAT

Bubbly Flow Through Fixed Beds: Microscale Experiments in the Dilute Regime and Modeling

M. L. Bordas, A. Cartellier, and P. Sechet
Laboratoire des Ecoulements Géophysiques et Industriel, INPG-UJF-CNRS, 1025 rue de la Piscine, 38400 St Martin d'Hères, France

Ch. Boyer
Institut Français du Pétrole, IFP-Lyon—Solaize, BP3, 69390 Vernaison, France

DOI 10.1002/aic.10980
Published online October 4, 2006 in Wiley InterScience (www.interscience.wiley.com).

In order to predict the pressure drop and the mean void fraction for bubbly flows in packed beds, a new one-dimensional (1-D) model is proposed. The balance equations for both phases are derived from local Eulerian two-fluid equations which are spatially averaged at a mesoscale, that is, at a length-scale large compared with the microscale that characterizes the fixed bed. This model, that differs from previous mechanistic models, has been supplemented by closure laws for the liquid-solid and the gas-liquid interactions, those structures account for the flow dynamics at the pore scale. It is first experimentally demonstrated that, in dilute conditions, the bubble-size distribution only depends on the pore size, when the later is smaller than the capillary length scale. It is also shown that the mean-bubble dynamics is similar to that of a slug, with a relative velocity at mesoscale linearly increasing with the liquid superficial velocity. Besides, that relative velocity monotonically increases with the gas flow rate ratio, a behavior that can be attributed to the formation of preferential paths for the gas phase. Concerning the liquid-solid interactions, the two-phase flow pressure drop scaled by its single-phase flow counterpart at the same superficial liquid velocity is predicted to linearly increase with the void fraction, with a prefactor evolving with the Capillary number. These closures prove consistent with available experiments, both in upward and in downward situations. Although these proposals deserve to be further tested over an extended range of flow parameters, this model paves the way to reasonably accurate predictions of bubbly flows in packed beds able to account for refined parameters related with the flow dynamics. © 2006 American Institute of Chemical Engineers *AIChE J,* 52: 3722–3743, 2006

Keywords: two-phase flow, packed bed, modeling, bubbles size, index matching, pressure drop

Introduction

Dispersed two-phase flows, such as bubbly flows are often exploited in chemical or bio-chemical processes, but their hydrodynamic is still not fully understood and their modeling still raises a number of unsolved issues.[1] This is notably so for two-phase reactors, such as bubble columns, and for three-phase packed reactors in which the solid phase is the catalysts.[2] Basically, these flows remain difficult to model because of the presence of complex interactions between phases. This article focuses on bubbly flows through a fixed bed of solids. More precisely, the beds considered hereafter are such that the interstices in the solid matrix which are available for the flow passage are smaller than (or at most of the same order as) the

Correspondence concerning this article should be addressed to P. Sechet at philippe.sechet@hmg.inpg.fr.

© 2006 American Institute of Chemical Engineers

Table 1. Summary of Some Existing Correlations for the Pressure Drop Due to Friction $(\Delta P/\Delta z)_f$ in Two-Phase Cocurrent Upflow in Fixed Beds

Authors	Operating Conditions	Proposed Correlations	Validity Conditions
Ford (1960)	$D_c = 0.045$ m $d_p = 1 \cdot 10^{-3}$ m Water/Air	$\left(\frac{\Delta P}{\Delta H}\right)_f = 0.0407 \rho_L g Re_L^{0.29} Re_G^{0.57} \left(\frac{\mu_L}{\mu_G}\right)^{0.28}$ $\left(\frac{\Delta P}{\Delta H}\right)_f = 0.0485 \rho_L g Re_L^{0.67} Re_G^{0.30} \left(\frac{\mu_L}{\mu_G}\right)^{0.80}$	$\varepsilon_{Lext} \leq 0.43\varepsilon$ $\varepsilon_{Lext} \geq 0.43\varepsilon$
Turpin et Huntington (1967)	$D_c = 0.051$ m, 0.102 m, 0.152 m $H = 2.13$ m $d_p = 7.6 \cdot 10^{-3}$ m, $8.23 \cdot 10^{-3}$ m Alumina cylinders $\varepsilon = 0.36$ Water/Air	$\left(\frac{\Delta P}{\Delta H}\right)_f = f_{LG} \frac{2\rho_G V_{SG}^2}{d_e}$ $\ln f_{LG} = 8.0 - 1.12(\ln Z) - 0.0769(\ln Z)^2 + 0.0152(\ln Z)^3$ $Z = \frac{R_{eG}^{1.167}}{R_{eL}^{0.767}} \left(\frac{\mu_w}{\mu_L}\right)^{0.9}, d_e = \frac{2\varepsilon}{3(1-\varepsilon)} d_p$	$0.3 \leq Z \leq 500$ $0.017 \leq V_{SL} \leq 5.3$ m/s $6.5 \cdot 10^{-3} \leq V_{SG} \leq 0.054$ m/s
Saada (1975)	$D_c = 0.045$ m $H = 0.40$ m $d_p = 5.14 \cdot 10^{-4}$ m, $9.74 \cdot 10^{-4}$ m, $2.06 \cdot 10^{-3}$ m Glass beads $\varepsilon = 0.40$ Water/Air	$\left(\frac{\Delta P}{\Delta H}\right)_f = 0.027 \rho_L g R_{eL}^{0.35} R_{eG}^{0.51} \left(\frac{d_p}{D_c}\right)^{-1.15}$ $\left(\frac{\Delta P}{\Delta H}\right)_f = 0.024 \rho_L g R_{eL}^{0.60} R_{eG}^{0.39} \left(\frac{d_p}{D_c}\right)^{-1.1}$	$R_{eG} \geq 0.44 R_{eL}^2 \left(\frac{d_p}{D_c}\right)^{0.38}$ $R_{eG} \leq 0.44 R_{eL}^2 \left(\frac{d_p}{D_c}\right)^{0.38}$
Barrios (1987)	$D_c = 0.050$ m, 0.150 m $H = 1.05$–1.13 m $d_p = 1.8 \cdot 10^{-3}$ m, $\varepsilon = 0.38$ $d_p = 2.7 \cdot 10^{-3}$ m, $\varepsilon = 0.32$ $d_p = 5.6 \cdot 10^{-3}$ m, $\varepsilon = 0.33$ Alumina spheres $d_p = 2.2 \cdot 10^{-3}$ m, $\varepsilon = 0.40$ Glass beads Water/Air Cyclohexane/N_2	$\left(\frac{\Delta P}{\Delta H}\right)_f = \left\{ A \left[\left(\frac{\Delta P}{\Delta H}\right)_L \cdot V_{SL} \right]^B + C \left[\left(\frac{\Delta P}{\Delta H}\right)_G \cdot V_{SG} \right]^D + < (L \cdot \beta + G \cdot \alpha) g \} \frac{E}{V_{SL} + V_{SG}}$ Bubbly flow: $A = 1.5$, $B = 1$, $C = 108.7$, $D = 0.395$, $E = 4.64$ Pulsed flow: $A = 13.8$, $B = 1$, $C = 5$, $D = 0.935$, $E = 1$ Spray flow: $A = 875.6$, $B = 0.735$, $C = 1.6$, $D = 0.935$, $E = 1$	$3.0 \cdot 10^{-3} \leq V_{SG} \leq 0.71$ m/s $2.4 \cdot 10^{-4} \leq V_{SL} \leq 0.058$ m/s
Ellman et col. (1988)	Numerous different conditions	$\left(\frac{\Delta P}{\Delta H}\right)_f = f_{LG} \frac{2G^2}{d_h \rho_G}$ $f_{LG} = 6.96(X_G \xi)^{-2} + 53.27(X_G \xi)^{-1.5}$ $X_G = \left(\frac{We_G}{We_L}\right)^{0.5}, d_h = \left[\frac{16\varepsilon^3}{9\pi(1-\varepsilon)^2}\right]^{0.33} d_p$ $\xi = \frac{Re_L^{0.25} We_L^{0.2}}{(1 + 3.17 Re_L^{1.65} We_L^{1.2})^{0.1}}$	Correlations developed for trickle-beds in the high interaction regime

$Re_L = \rho_L \cdot V_{SL} \cdot d_p/\mu_L$. $Re_G = \rho_G \cdot V_{SG} \cdot d_p/\mu_G$.

capillary length. In industry, this type of reactor is often preferred to mobile beds because of its high-conversion efficiency for rather low investments and maintenance costs. Yet, reliable tools are lacking for dimensioning and optimizing these reactors as well as for explaining some of their malfunctions. An accurate modeling of the hydrodynamics of bubbly flows in packed beds is, therefore, needed to ensure a better control of the operating conditions.

The main quantities relevant for operating fixed-bed reactors are the pressure drop along the bed which is needed for their design, and the void fraction and/or the interfacial area between phases which control the efficiency of the chemical reactions between species. Previous studies have mainly focused on the determination of these quantities. However, due to the large number of parameters involved *a priori* in the flow control, such experiments led most of the time to empirical correlations which cannot be extrapolated to different operating conditions with confidence. As an example, some available correlations for the pressure drop are presented in Table 1, where the quantity

$$\left(\frac{\Delta p}{\Delta z}\right)_f = \left(\frac{\Delta p}{\Delta z}\right)_t - ((1-\alpha)\rho_L + \alpha\rho_G)\, g$$

represents the contribution of friction to the pressure drop. It equals the total pressure drop (indexed by t) diminished by the hydrostatic head associated with the mean density of the two-phase mixture (here α represents the void fraction, ρ_L is the liquid density, ρ_G the gas density, and g the gravity). Clearly, strong disagreements arise between these proposals. As shown in Table 1, these correlations use different sets of control parameters indicating that no unified model is available for such two-phase flows. Moreover, the spread is large between the predictions as shown Figure 1, where the correlations of Table 1 have been plotted for the same operating conditions.

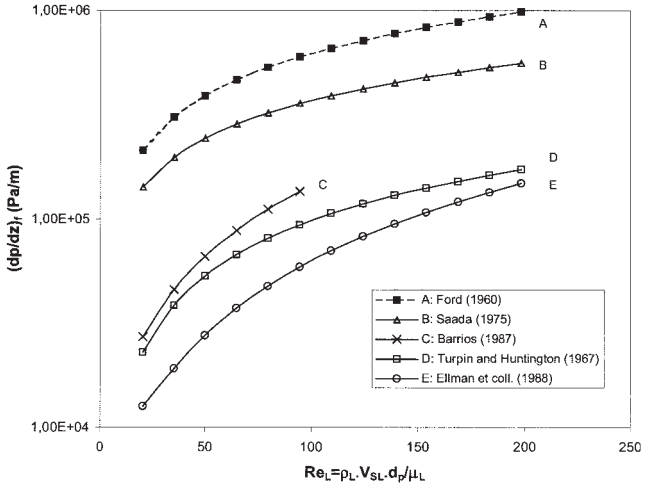

Figure 1. Comparison between some pressure drop correlations proposed in the literature.

(Air-water cocurrent flows in fixed beds consisting of spherical beads. Bead dia. $d_p = 2$ mm, $D_c = 45$ mm, $\varepsilon = 0.36$, $Re_G = \rho_G V_{SG} d_p/\mu_G = 20$).

Here, $V_{SL} = Q_L/S$ (respectively, $V_{SG} = Q_G/S$) represents the liquid (respectively, the gas) superficial velocity, D_c the column diameter, S the column cross-section area, d_p the diameter of the solid particles constituting the fixed bed, ε the porosity. In addition, drastically different pressure drop behaviors are reported in the literature. For example, 3 found that the pressure drop is much higher in small columns than in large ones, 4 did not mention any influence of the column size, and 5 observed an increase of the pressure drop with the column diameter. Also, some authors[6] observed an increase of the pressure drop with the particle diameter: such a trend contradicts most of the reported works and is somewhat hardly explainable.

Mechanistic model of Attou and Ferschneider

All the above mentioned correlations are purely empirical, and more mechanistic approaches must be considered in order to derive predictive formula. The first serious attempt to interpret the pressure drop in terms of a force balance is due to Attou and Ferschneider.[1] These authors derived a 1-D model (named AF-model in the sequel) for cocurrent bubbly flows in which the physical origin of the pressure drop is due to the coexistence of four interaction forces: the friction force density between the liquid and the solid f_{LS}, the friction force density between the liquid and the column wall f_w, the interaction force density between the liquid and the gas phases f_{LG}, and the interaction force density between the gas and the solid phases f_{GS}. For bubbly flows, the solid is usually entirely wetted by the liquid (strong preferential wetting), so that f_{GS} can be neglected. With the reactor axis z directed along gravity, the 1-D momentum equations of the AF-model write for each phase

$$Liquid: -(1-\alpha)\frac{dp}{dz} = (1-\alpha)\rho_L g + f_{LS}^{AF} + f_w - f_{LG}^{AF} \quad (1)$$

$$Gas: -\alpha\frac{dp}{dz} = \alpha\rho_G g + f_{LG}^{AF} \quad (2)$$

where both the pressure and the void fraction are assumed to be uniform over any cross-section of the reactor. In the above equation, z is directed along the main flow direction. The superscript AF refers to the force densities defined by Attou and Ferschneider. To close their model, Attou and Ferschneider expressed the total friction between the liquid and the solid phase, namely f_{LS} (for large columns, the contribution of f_w is negligible compared with that of f_{LS}), by modifying the Ergun equation[7] derived for one-phase flow through packed beds. Such an approach was previously used by Benkrid et al.[8] who adapted the Ergun equation to two-phase flows by accounting for the volume occupied by the gas in the free space as if the gas was merely affecting the porosity. Denoting ψ the ratio between the two-phase flow pressure drop, and the pressure drop for the corresponding monophasic flow at the same liquid superficial velocity, that is, $\psi = f_{LS}/f_{LS,1\varphi}$, the model of Benkrid et al. writes

$$\psi = \frac{1}{(1-\alpha)^3} \quad (3)$$

where $f_{LS,1\varphi}$ is given by the Ergun equation

$$f_{LS,1\varphi} = A\frac{(1-\varepsilon)^2}{\varepsilon^3 d_p^2}\mu_L V_{SL} + B\frac{(1-\varepsilon)}{\varepsilon^3 d_p}\rho_L V_{SL}^2 \quad (4)$$

In the earlier equation, the parameters A and B recommended by Ergun are usually replaced by those, more reliable, of 9. In addition to the change in the "apparent" porosity, Attou and Ferschneider took into account the liquid residence time $(1-\alpha)$ at a given location within the pore. Consequently, their proposal is equivalent to multiplying the closure of Benkrid et al. by $(1-\alpha)$, leading, thus, to

$$\psi = \frac{1}{(1-\alpha)^2} \quad (5)$$

Concerning the interaction between the gas and the liquid, Attou and Ferschneider modeled the gas-liquid momentum exchange f_{LG} as the number density times the drag force on a bubble. The later was expressed by way of a drag coefficient C_D which was determined from correlations valid for single inclusions in an infinite medium (namely, at low particulate Reynolds numbers, the Hadamard–Rybczynski formula derived for a clean spherical bubble and, at large particulate Reynolds numbers, the Newton law for solid inclusions).

The evaluation of C_D requires the knowledge of the bubble size. As no data were available concerning the size and the shape of bubbles in fixed beds, Attou and Ferschneider assumed that the maximum bubble diameter is controlled by turbulent breakup and, following[10], they related the bubble size with the dissipation in the liquid.

They also accounted for the influence of neighbor bubbles by introducing a hindering coefficient, those expression was taken from[11]: at small or moderate gas fraction (that is, in bubbly

flows), the actual drag compared with the drag on an isolated bubble was increased by a factor $1/(1-\alpha)$ while in dense conditions, it was decreased by a factor $(1-\alpha)^3$.

Discussion of the AF-model

The originality of the AF-model arises from the particular effort devoted to the physical modeling of the interaction phenomena between the various phases. Moreover, it does not require any adjustable parameter. Yet, both the structure of that model and the proposed closures need to be revisited. Indeed, the AF-model suffers from a serious drawback in terms of the mechanism driving the bubble motion. That can be readily seen from Eq. 2 that states that the average drag force on the bubble balances the pressure gradient in the liquid. This statement is not compatible with the classical Basset-Boussinesq-Oseen equation describing the motion of a single bubble in a large volume of liquid. Indeed, the dynamic equilibrium of an isolated spherical bubble of radius a, volume $V_p = (4/3)\pi a^3$, and negligible density obeys

$$\mathbf{F^*} = (\nabla p - \nabla \cdot \tau)V_p = -\rho_L(D\mathbf{v}/Dt - \mathbf{g})V_p \qquad (6)$$

where $\mathbf{F^*}$ denotes the resisting force exerted by the liquid on the inclusion. Equation 6 means that the driving term is the fluid acceleration $D\mathbf{v}/Dt$ diminished by the gravitational acceleration, or equivalently the pressure gradient in the continuous phase ∇p less the viscous stress contribution $\nabla \cdot \tau$. In absence of fluid acceleration, the resistive force $\mathbf{F^*}$ on the bubble, and along the direction of gravity balances the buoyancy $\rho_L g V_p$. As the two-fluid momentum balance equations for packed beds should remain valid in the limit of very large pores (or even a duct), the gas momentum balance proposed by Attou et al. states that the resisting force is proportional to the pressure gradient: this is incorrect. On the other hand, the liquid momentum balance of the AF-model is correct in its structure, and that feature partly explains why the AF-model was reasonably successful in predicting the pressure drop, since the later is mainly governed by the liquid friction on the solid boundaries. Concerning the closures, a number of assumptions appear to be quite arbitrary, if not incorrect. First, the drag coefficients exploited by Attou and Ferschneider do not account for the confinement, while it is well known that the later drastically alters the drag force (see, for example,[12]). Also, strong shape distortions are to be expected for bubbles of the order of, or larger than, the pore size (this is particularly valid for pore sizes smaller than the capillary length) while the closures selected by Attou and Ferschneider only apply to spherical inclusions. In addition, at the pore scale, the bubbles are subject to strong accelerations and decelerations, so that added mass and possibly history force are expected to significantly contribute to the resisting force exerted on the bubble. Concerning the hindering effect, some interactions between bubbles may well be present in packed beds, but they certainly differ from the interactions arising in a cloud of bubbles, free to move in a large volume of liquid. Let us recall that the closures proposed by[13] were derived from gas-liquid two-phase flows in pipes those size was much larger than the capillary length: there is no physical reason why these expressions should remain valid in strongly confined systems, such as the fixed beds considered here. Finally, the bubble size is said to be controlled by turbulent breakup. Although this could be valid for some flow regimes, that mechanism is certainly not always active owing to the relative importance of viscous stresses in packed beds. Instead, one expects shear breakup combined with snapoff to be the dominant mechanism over a significant range of flow conditions.[14,15] Moreover, and whatever the breakup mechanism considered, the bubble-size distribution in such systems is still unknown.

Owing to the earlier comments, it is not ascertained whether a model based on a unique bubble size is adapted to describe dispersed flows in packed beds. Also, one may wonder whether the interfacial momentum exchanges can be adequately represented by a steady-state drag coefficient. In order to address these questions, a detailed investigation of dispersed gas-liquid flows in packed beds has been undertaken that combines the derivation of a new 1-D average formulation with refined experimental investigations performed in the dilute limit. The proposed model follows a different approach from the AF-model: indeed, it is grounded on local instantaneous Eulerian equations for the two-flowing phases. The later are taken from the two-fluid hybrid formulation developed by Achard and Cartellier[16] that mixes concepts inspired from the kinetic theory with continuum mechanics. These local equations happen to be valid everywhere in the interstices: they are then spatially averaged over a volume whose characteristic length scale is larger than the solid particles constituting the porous medium in order to produce a mesoscale two-fluid model. Closure laws are again required to complete these averaged equations. Yet, and as it will be shown hereafter, that new approach allows a closer connection between these required closures and the flow dynamics at small scale.

The article is organized as follows. The first section is devoted to the presentation of the 1-D model. The hybrid model is first summarized and by averaging, the mesoscale two-fluid formulation is established. In the second section, refined experimental investigations are presented that provide the actual size distribution, as well as the mean relative velocity of bubbles in the dilute limit. It is shown that the bubble-size distribution reaches a frozen state at some distance from the injection, and that its extend remains limited. Consequently, it seems legitimate to consider a unique bubble diameter, representative of the interfacial momentum exchange. Within that framework, global experimental data from the literature are revisited in the third section, and are exploited to validate a new closure proposal for the liquid-solid interaction. The later happens to significantly differ from that introduced in the AF-model. A companion paper will expand that analysis to higher void fractions.

One Dimensional Modeling of Bubbly Flows through Fixed Bed

Hybrid approach

A model is established on the basis of the so-called hybrid approach. This formulation has been developed in order to improve the capabilities of the two-fluid Eulerian description by systematically transposing information obtained at a microscopic level (typically at the scale of a bubble) to the macroscopic level (such as the reactor scale). In that scope, a continuum mechanistic description for the liquid phase is mixed with a kinetic theory treatment for the dispersed phase. The

equations for the mean variables are obtained from an ensemble average over all possible configurations of the dispersed phase. The development of these general equations is made possible by making some restrictions: the bubbles are spherical and their size is fixed (the radius is noted a) and phenomena, such as coalescence, breakup or collisions between inclusions are excluded. Strictly speaking, no turbulence in the liquid phase was considered, but the resulting equations are valid for turbulent conditions as well. The detailed derivation of the hybrid formulation can be found in[16,17]. Only its main features are summarized here later.

The hybrid model consists in a double hierarchy of coupled equations, one for each phase. Only the unconditional equations are exploited hereafter. The later govern the mean velocity $\mathbf{v}$, and the mean pressure p in the continuous phase: these variables are the same as those introduced in standard two-fluid Eulerian formulations.[11,18] On the opposite, the dispersed phase is described by variables relative to the inclusions center of mass: they concern the mean number density $\phi^{(1)}(\#/m^3)$, and the average translational velocity $\mathbf{u}$ of the inclusions (rotation is excluded here). In particular, the void fraction at a location $\mathbf{x}$ is related with the number density by way of a spatial integration over all the bubble positions contributing to the presence of the gas phase at a location $\mathbf{x}$. For a monodispersed-size distribution, one has

$$\alpha = \frac{4}{3}\,\pi a^3\left[\,\phi^{(1)} + \frac{1}{10}\,\nabla^2\phi^{(1)} + \ldots\right] \tag{7}$$

The velocity $\mathbf{v}$, and pressure p in the liquid phase are governed by the following continuity (Eq. 8), and the momentum (Eq. 9) equations

$$-\frac{\partial\alpha}{\partial t} + \frac{\partial}{\partial\mathbf{x}}\cdot[(1-\alpha)\mathbf{v}] = 0 \tag{8}$$

$$\rho_L\frac{D\mathbf{v}}{Dt} = -\nabla p + \nabla\cdot\tau + \rho_L\mathbf{g} + \frac{1}{(1-\alpha)}[\nabla\cdot\pounds + \mathbf{M} - \rho_L\nabla\cdot\mathbf{A}_{vv}] \tag{9}$$

In Eq. 9, $(D/Dt) = (\partial/\partial t) + \mathbf{v}\cdot(\partial\mathbf{v}/\partial\mathbf{x})$ is the particulate derivative following the continuous phase. $\tau = 2\mu_L[\partial\mathbf{v}/\partial\mathbf{x}]$ is the viscous stresses tensor where $[\cdot]^s$ denotes the symetrical part of the tensor. The equation (Eq. 9) is a Navier-Stokes equation that includes three-source terms, due to the two-phase character of the flow, namely

—the extra-deformation tensor £ exactly given by

$$\pounds(\mathbf{x}) = 2\mu_L\int_{S_b(x)}\mathbf{n}_c\mathbf{v}^*(\mathbf{x}|\mathbf{x}+a\mathbf{n}_c)\phi^{(1)}(\mathbf{x}+a\mathbf{n}_c)a^2d\Omega \tag{10}$$

$\pounds(\mathbf{x})$ can be closed when a stick boundary condition applies at the interface, such as in strongly contaminated systems.[16,19]

—the interfacial momentum source $\mathbf{M}$, exactly given by

$$\mathbf{M}(\mathbf{x}) = \int_{S_b(x)}\mathbf{n}_c\cdot[-p^*\mathbf{I} + 2\mu_L\mathbf{D}(\mathbf{v}^*)]\phi^{(1)}(\mathbf{x}+a\mathbf{n}_c)a^2d\Omega \tag{11}$$

In the earlier two equations, $S_b(x)$ denotes the sphere centered at $\mathbf{x}$, and of radius a, $\mathbf{n}_c$ is the unit vector normal to the surface S_b, $\mathbf{I}$ is the unit tensor, and $\mathbf{D}$ is the symetrical part of the gradient tensor.

The "star" quantities $\mathbf{v}^* = \mathbf{v}(\mathbf{x}|\mathbf{x}^\circ) - \mathbf{v}(\mathbf{x})$, and $p^* = p(\mathbf{x}|\mathbf{x}^\circ) - p(\mathbf{x})$ are the perturbed velocity and pressure fields, respectively. $\mathbf{v}^*$ is the difference between the averaged velocity $\mathbf{v}(\mathbf{x}|\mathbf{x}^\circ)$ at the location $\mathbf{x}$ conditioned by the presence of an inclusion at the location $\mathbf{x}^\circ$, and the unconditional-mean velocity $\mathbf{v}(\mathbf{x})$ at $\mathbf{x}$. p^* has a similar definition. Equation 11 states that the momentum source for the liquid at a given location $\mathbf{x}$ results from the stresses due to the perturbed field evaluated at the interface, and integrated over all possible bubbles location $\mathbf{x}^\circ = \mathbf{x} + a\mathbf{n}_c$, such as their interface touches $\mathbf{x}$ (see Figure 2). Each eligible bubble location $\mathbf{x}^\circ$ is weighted by the number density $\phi^{(1)}$ at that point.

—the cofluctuation of the liquid velocity $\mathbf{A}_{vv}$: that term represents the turbulence, as well as the pseudo-turbulence induced by the bubbles in the continuous phase.[20] The closure of this term is not discussed further since it will disappear during the derivation of 1-D equations in fixed beds.

For the dispersed phase, the number density $\phi^{(1)}$, and the average translation velocity $\mathbf{u}$ are governed by the following continuity and momentum equations

$$\frac{\partial\phi^{(1)}}{\partial t} + \frac{\partial}{\partial\mathbf{x}}\cdot\phi^{(1)}\mathbf{u} = 0 \tag{12}$$

$$\rho_G\frac{D\mathbf{u}}{Dt} + (1+R_1)[\nabla p - \nabla\cdot\tau] - \rho_G\mathbf{g} = -\frac{\rho_G}{\phi^{(1)}}\nabla\cdot\mathbf{A}_{uu} + \frac{\mathbf{F}^*}{V_p} \tag{13}$$

R_1 represents the operator $\Sigma_{n\geq1}\,6(n+1)a^{2n}\Delta^n/(2n+3)!$, where Δ^n means n applications of the Laplacian operator. $\mathbf{A}_{uu}$ accounts for cofluctuations of the dispersed-phase velocity. For bubbles (that is, $\rho_G \to 0$), Eq. 13 simplifies into

$$(1+R_1)[\nabla p - \nabla\cdot\tau] = \frac{\mathbf{F}^*}{V_p} \tag{14}$$

indicating that the bubble dynamics consists in a balance between the driving force set by the mean motion in the liquid phase—the lefthand side of Eq. 14—and the mean resistive force $\mathbf{F}^*$ exerted on the inclusion by the continuous phase perturbed field. $\mathbf{F}^*$ equals the integral over the interface of the stress field associated with the disturbance $\mathbf{v}^*$, p^*, namely

$$\mathbf{F}^*(\mathbf{x}) = a^2\int_{S_b(x)}[p^*\mathbf{n}_c - 2\mu_L\mathbf{n}_c\cdot\mathbf{D}(\mathbf{v}^*)(\mathbf{x}-a\mathbf{n}_c|\mathbf{x})]d\Omega \tag{15}$$

If an analytical solution is available for the fields $\mathbf{v}^*$, p^*, as for the slow motion of a bubble in an infinite medium, then the earlier equation directly provides the mean resisting force (such

as the drag, the lift, and so on . . .). In general, the perturbed fields have to be extracted from direct numerical simulations of an adequately selected set of microproblems, such as, for example, the flow around a single bubble, in an interstice (the equations governing $\mathbf{v}^*$ and p^* are not detailed here—see[16,17,21,22]). In the same way, the interfacial momentum exchange as given by Eq. 11 can be directly computed from solved microproblems if the number density is known. The presence of the variable $\phi^{(1)}$ in the expression of $\mathbf{M}(\mathbf{x})$ is the clear indication that the system of phasic equations is strongly coupled. Alternatively, the interfacial momentum exchange can be related with the mean resisting force. Indeed

$$\mathbf{M} = \sum_{m=0}^{\infty} a^m \frac{\partial^m}{\partial \mathbf{x}^m} \otimes^m [\phi^1 \mathbf{M}^*_{m+1}] = \phi^{(1)} \mathbf{M}^*_1 + a \frac{\partial}{\partial x} [\phi^{(1)} \mathbf{M}^*_2] + \mathbf{Q}^* \quad (16)$$

where $\mathbf{M}^*_{m+1}$ is the first-order force multipole defined as

$$\mathbf{M}^*_{m+1} = a^2 \frac{(-1)^{(m+1)}}{m!} \int_{S(\mathbf{X})} \mathbf{n}^{m+1} \times [-p^* \mathbf{I} + 2\mu_L \mathbf{D}(\mathbf{v}^*)](\mathbf{x} + a\mathbf{n}|\mathbf{x}) d\Omega \quad (17)$$

The first and main contribution to the interfacial momentum source at $\mathbf{x}$, $\mathbf{M}^*_1$, happens to be equal to the opposite of $\mathbf{F}^*$ exerted on a particle centered at $\mathbf{x}$. The second term $\mathbf{M}^*_2$ accounts for the torque on the particle and for the unconditional velocity deformation in the continuous phase. The remaining contribution $\mathbf{Q}^*$ groups terms of order $(a/L)^m$, where a is the particle radius, and L the characteristic length-scale of the unconditional continuous flow field. If $a/L \ll 1$, the equation (Eq. 16) reduces to

$$\mathbf{M} = -\alpha \mathbf{F}^*/V_p = -\phi^{(1)} \mathbf{F}^* \quad (18)$$

which is the usual expression introduced in most Eulerian two-fluid formulations. That equation simply states that the momentum source for the liquid is the number of (small) particles per unit volume times the external force on an inclusion. Yet, the closure in the earlier form is valid only if the scale separation is effective, that is for bubbles small enough compared with the length scale L of the mean-liquid flow field. Anticipating on the next paragraph, it is expected that such a condition is usually not ascertained in fixed beds because L becomes of the order of the pore scale. In that case, all the contributions should be taken into account in Eq. 16, or alternately one should directly use the equation (Eq. 11). Similarly, the operator R_1 that enters the gas momentum equation contributes at the order $O(a/L)^2$ to the balance: its contribution arises from liquid pressure or velocity nonuniformity at the scale of the particle size. Again, if the scale separation is not effective, its contribution cannot be neglected.

Application to dispersed bubbly flow in porous media: spatially averaged equations

The local instantaneous equations of the previous section are thereafter applied to a bubbly flow through a homogeneous porous medium. It is assumed, as confirmed by visual observations in all our experiments, that there is no direct contact, and, consequently, no momentum exchange, between the gas and the solid. This statement is valid whenever the liquid preferentially wets the solid. Therefore, the equations presented in the previous paragraph are valid everywhere in the interstices. Yet, the resolution of these equations supplemented with the proper boundary conditions is a formidable task that would require a huge amount of microproblems to be solved. For two-phase flows in a duct that program is not yet completed.[23] For three-phase flows, the situation is even more complex. Indeed, at the bubble scale (microscale), one expects all the ensemble averaged quantities used in the hybrid model (such as the relative velocity $\mathbf{u}_r$) to be functions of the space coordinates. In particular for the relative velocity, the drag coefficient changes drastically with the ratio between the bubble diameter and the pore size (both due to confinement and to interface deformation). Also, added mass (and possibly history effect) are significant as the carrier fluid is subject to strong acceleration and deceleration at the pore scale. Thus, the resolution of both velocity fields $\mathbf{v}(x)$ (continuous phase), and $\mathbf{u}(x)$ (dispersed phase) is a very complex problem that requires in particular a detailed specification of the porous media characteristics, such as the pore size, geometry, tortuosity . . . . Although feasible in principle using direct numerical simulations and interface tracking techniques (see, for example,[24]), such a work program is for the long run. A simplified 1-D description, adapted to engineering requirements, is more urgently needed.

Averaging at mesoscale

In order to derive a 1-D model describing two-phase bubbly flows in packed beds, composed of equal sized beads, a spatial averaging of the local fields, such as $\mathbf{v}$, p; ϕ, and $\mathbf{u}$ is performed over a volume those characteristic length scale l is large compare to the beads diameter (typically l should be about several, $\sim$10 beads). In the perspective of producing local descriptions (local at a scale l), this size must also be kept smaller than the reactor dimension. After averaging, we seek to retrieve phasic flow fields at mesoscale which are unidirectional, stationary, and fully-developed. The selected volume, sketched in Figure 3b, is basically a cube of cross-section area S, and of extent dz, where z is directed along the main flow direction (that corresponds to the duct or the vessel axis). The control volume itself corresponds to the intersticial volume V_o enclosed in that cube (that is, the volume occupied by the fluid phase). V_o is bounded by the closed surface S_o selected as follows: along a side of the "cube" those normal is n_i ($i = x$, y, or z), the boundary is the flat surface normal to n_i excepts, where it intercepts a bead, in which case, the boundary coincides with the bead surface. Such a choice is always possible. The volume averaging operator, noted $\langle \cdot \rangle$, is defined as

$$\langle f \rangle = \frac{1}{V_o} \int_{V_o} f dx \quad (19)$$

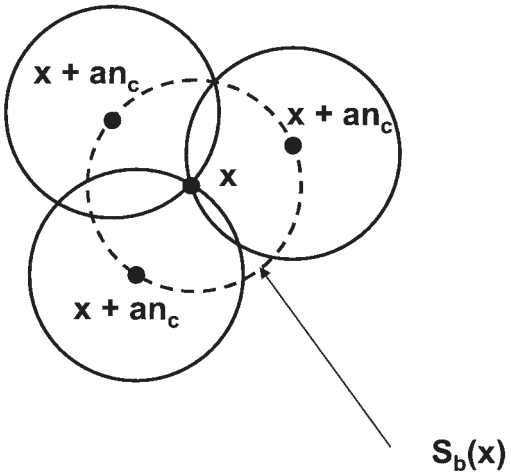

Figure 2. Evaluation of the interfacial momentum source at *x* for the liquid phase.

A surface average, performed over the fluid area S_F normal to the direction z, is also required. It is denoted with an overbar, as follows

$$\bar{f}_i = \frac{1}{S_{iF}} \int_{S_{iF}} f dx \tag{20}$$

Because of the fully-developed assumption at mesoscale, volume and surface average are identical for the void fraction, and the phasic velocities. Yet, the surface average is required for the pressure.

The volume average is then applied to the balance equations provided by the hybrid model. For sake of simplicity, absolute pressure effects have been discarded so that the gas density remains constant (and such that $\rho_G \ll \rho_L$). The details of the derivation of the mesoscale model are given in Appendix A. The main conclusions are the following. The continuity equations at mesoscale are identically satisfied because of the unidirectional, fully developed, and stationary assumptions introduced for the flow at mesoscale. When neglecting the friction on the lateral fluid boundaries (or even on the outer walls of the vessel) compared with f_{LS}, the phasic momentum equations in the axial direction write

$$-\frac{d\bar{p}}{dz} = \rho_L g + f_{LS} - \langle M_z/(1-\alpha)\rangle \tag{21}$$

$$-d\bar{p}/dz = f_{LS} + \langle R_1[\nabla p - \nabla \cdot \tau]\rangle - \langle F_z^*/V_p\rangle \tag{22}$$

where $f_{LS} = -\int_{S_{obeads}} (-p\mathbf{n} + \tau \cdot \mathbf{n})_z$ is the z-component of the force density per unit intersticial volume, exerted by the liquid on the fixed bed. The earlier equations are applicable for any orientation relative to gravity, provided that z is directed along the main flow direction, and that g is understood as $g = -|g|cos(\mathbf{n}_z, \mathbf{g})$. So doing, both $-(d\bar{p}/dz)$ and f_{LS} are positive. The definitions of all the terms appearing under the volume averaging operator have already been provided.

Exploitation of the balance equations at mesoscale

To discuss these axial momentum balance equations at mesoscale, let us first consider bubbles whose size is much smaller than the pore scale. When $a/\delta \ll 1$, the scale separation is effective so that a bubble perceives a homogeneous liquid field. Thus, the correction term related with the operator $\langle R_1[\nabla p - \nabla \cdot \tau]\rangle$ becomes negligible compared with the generalized Archimedian force $\langle V_p[\nabla p - \nabla \cdot \tau]\rangle$. In addition (and provided that the bubble center is not too close from a solid surface to avoid local gradients at a scale comparable with the bubble size), the momentum exchange $\mathbf{M}$ reduces to a monopole, and the closure (Eq. 18) allows to relate M_z with the mean resisting force component along the flow direction z. Indeed, identifying the liquid-gas force density with the M_z term, one has

$$f_{LG} = -\langle M_z/(1-\alpha)\rangle = \langle \alpha(F_z^*/V_p)/(1-\alpha)\rangle = \bar{\alpha}\langle F_z^*/V_p\rangle/(1-\bar{\alpha}) \tag{23}$$

where the last equality is expected to hold because of the assumed homogeneities of the porous medium, and of the flow. Finally, the phasic momentum balances write

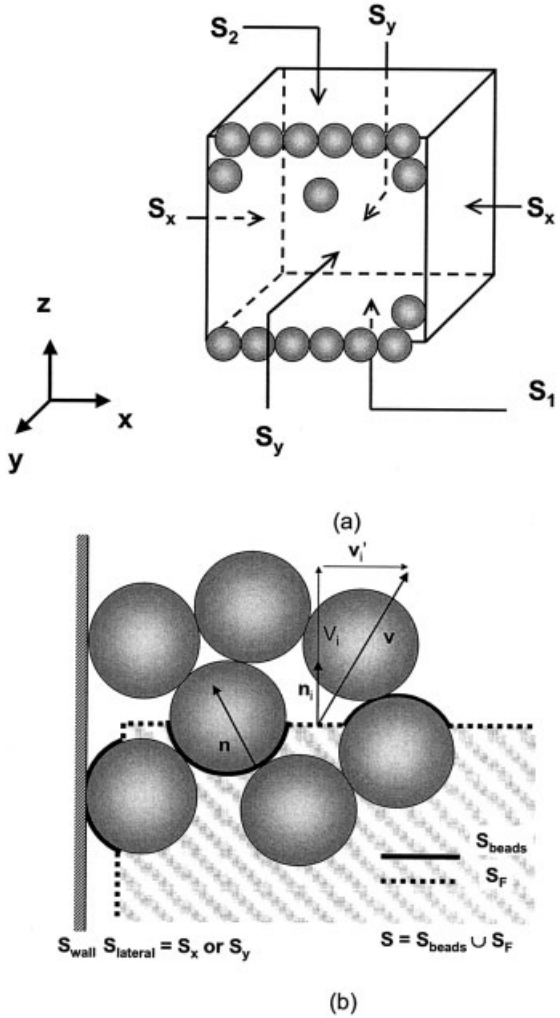

Figure 3. Integration volume and notations.

$$-\frac{d\bar{p}}{dz} = \rho_L g + f_{LS} + f_{LG} \tag{24}$$

$$-d\bar{p}/dz = f_{LS} - \frac{(1-\bar{\alpha})}{\bar{\alpha}} f_{LG} \tag{25}$$

which can be rewritten

$$-\frac{d\bar{p}}{dz} = (1-\bar{\alpha})\rho_L g + f_{LS} \tag{26}$$

$$f_{LG} = -\bar{\alpha}\rho_L g \tag{27}$$

The first equality provides the axial-pressure drop as the sum of the liquid friction on the beads and the weight of the two-phase mixture. The second one gives the interfacial momentum exchange: that result is as expected since the total force on a massless bubble is zero so that **F*** balances $V_p \rho_L g$. This second equation allows to compute the bubble relative velocity when the expression of the drag force is available. The earlier set of equations is formally the same as the one derived for bubbly flows in large ducts.[25] As it has already been pointed out, when compared with the Eq. 27, the AF-model that predicts

$$f_{LG}^{AF} = -\bar{\alpha}\frac{d\bar{p}}{dz} = \bar{\alpha}(1-\bar{\alpha})(\rho_L g + f_{LS}^{AF}) \tag{28}$$

is not compatible with the dynamics of small bubbles. Let us turn now toward the case where a/δ is no longer negligible, and possibly even larger than unity. Two difficulties have to be faced. First, the relationship between the interfacial momentum transfer **M** and the resisting force **F*** is no longer straightforward since higher-order contributions in Eq. 16 become significant. Second, the perturbations v^* and p^* of the liquid flow field due to the motion of bubbles in the pores become large, eventually of the same order or higher than the unconditional fields. Hence, the force driving the bubble motion involves a significant contribution due to flow inhomogeneities, represented by the term $\langle R_1[\nabla p - \nabla \cdot \tau]\rangle$. It is, thus, no longer possible to simply relate the gas-liquid interaction terms appearing in the two-phasic momentum equations. One recovers here the general situation of two-fluid approaches where the contribution $\langle R_1[\nabla p - \nabla \cdot \tau]\rangle$, as well as the momentum source for the liquid **M** cannot be simply expressed in terms of the mean variables. The later difficulty has already been pointed out for the treatment of wall regions for bubbly flows in ducts.[26,27] One is, therefore, left with the equations under the form Eqs. 21 and 22, which, in principle, can be solved with the help of direct numerical simulations of the perturbed motion. These equations can be rewritten

$$-\frac{d\bar{p}}{dz} = \rho_L g + f_{LS} - \langle M_z/(1-\alpha)\rangle \tag{29}$$

$$\langle F_z^*/V_p\rangle - \langle M_z/(1-\alpha)\rangle = -\rho_L g + \langle R_1[\nabla p - \nabla\cdot\tau]\rangle \tag{30}$$

In the dilute limit, M is $O(\alpha)$, so that the pressure gradient is still controlled by the liquid-solid interaction f_{LS}. Yet, the correction due to the $\langle M_z/(1-\alpha)\rangle$ term may not be that small at larger gas content. Thus, interpreting the quantity dp/dz_f defined in the introduction (and accessible from experimental data) as the liquid-solid force density may be partly incorrect. The second equation cannot be simplified either. Although in the dilute limit $\langle M_z/(1-\alpha)\rangle$ is negligible compared with $\langle F_z^*/V_p\rangle$, the term $\langle R_1[\nabla p - \nabla \cdot \tau]\rangle$ cannot be eliminated using scaling arguments. Indeed, anticipating on the next section, the disturbed pressure field in the vicinity of a large bubble scales as σ/δ, where δ is a characteristic dimension of the pores, so that $\langle R_1[\nabla p - \nabla \cdot \tau]\rangle$ compared with $\rho_L g$ is of the order $(a_c/\delta)^2$. For the fixed beds considered here, this ratio is of order unity or larger. Thus, and contrary to the case of very small bubbles, gravity is not the only ingredient governing the bubble motion. This is to be expected since, as already mentioned, the bubbles are strongly deformed, are subject to strong acceleration/deceleration and also may create preferential paths inside the porous medium.

Kinematic approach

As the complexity of the gas momentum equation precludes any simple analytical solution for the bubble-relative velocity, we sought a way to by-pass that difficulty. Following the approach of [25] for a bubbly column, the mean void fraction can be related with the mean relative velocity thanks to kinematic considerations. The mesoscale average axial velocities of the gas phase $\langle u\rangle$ and of the liquid phase $\langle v\rangle$, are first expressed vs. the volumetric flow rate for the liquid Q_L, and for the gas Q_G

$$\langle u\rangle = \frac{Q_G}{\langle\alpha\rangle\varepsilon S} \tag{31}$$

$$\langle v\rangle = \frac{Q_L}{(1-\langle\alpha\rangle)\varepsilon S} \tag{32}$$

where S is the total cross-section of the system (the reactor), and where ε is the bed porosity. The mean relative velocity at mesoscale is defined as

$$U_r = \langle u\rangle - \langle v\rangle \tag{33}$$

Introducing the volumetric flow rate ratio $\beta = [Q_G/(Q_G + Q_L)]$, and combining the above equations, one gets

$$\left[\frac{\beta}{1-\beta} - \frac{\langle\alpha\rangle}{1-\langle\alpha\rangle}\right] = \frac{\langle\alpha\rangle\varepsilon U_r}{V_{SL}} \tag{34}$$

where $V_{SL} = (Q_L/S)$. The Eq. 34 univocally relates the mean void fraction $\langle\alpha\rangle$ with the volumetric flow rate ratio β for given operating conditions provided that the mean relative velocity at mesoscale is known by independent means. Alternately, the kinematic relationship (Eq. 34) combined with void fraction measurements provides the mean relative velocity at mesoscale: this procedure is exploited in the section "*Relative velocity at mesoscale*" in order to examine the behavior of U_r in various flow conditions. Finally, in order to supplement the

gas momentum balance (Eq. 22), it would be worthwhile to relate U_r with the average resisting force density on a bubble $\langle \mathbf{F}^*/V_p \rangle$.

At this stage, the 1-D model that has been established gives access to the pressure drop, and to the void fraction for gas-liquid flows in packed beds provided that closure laws are available for the liquid-gas interfacial momentum transfer density f_{LG}, and for the mean-relative velocity at mesoscale U_r. In the last section, and starting from the flow dynamics at small scale, new expressions will be proposed for these closures. Beforehand, some central questions have to be addressed concerning the size of bubbles in packed beds. First, a basic assumption of our model is that the bubble size does not evolve in time, nor in space, that is, that breakup and coalescence processes are absent. Second, even if the size distribution is frozen, it may vary with flow conditions. If so, an extra closure would be required for the bubble size. A third, but less critical issue, concerns the hybrid model itself. Strictly speaking, that model has been formulated for a monodispersed-size distribution, and for spherical bubbles. Extensions to polydispersed conditions, as well as to nonspherical shapes are relatively straightforward, although they introduce extra complexity and, thus, require extra information. In particular, the momentum balances for both phases would remain the same, the various involved quantities being further averaged over the actual size and shape distributions. Such a process would also complexify the connection between the force on a bubble and the liquid-gas momentum exchange (see the section "*Averaging at mesoscale*"). Yet, we choose here to replace the gas momentum equation by the kinematical equation (Eq. 34) in which the bubble dynamics is hidden in U_r. That relationship still holds for an extended-size distribution $pdf(d)$, provided that the gas flux is kept constant, that is, provided that the mesoscale gas velocity $\langle u \rangle$ is determined as follows

$$\langle u \rangle = \frac{1}{d_{30}^3} \int \langle u \rangle(d) d^3 pdf(d) dd \tag{35}$$

where $d_{30}^3 = \int d^3 pdf(d) dd$.

Hence, the most critical questions to be addressed concern the bubble size and the possible influence of coalescence or breakup processes. No information is available about the size of bubbles in fixed beds, some experimental investigations have been undertaken on this question: the procedure and the results are detailed in the next section.

Behavior of isolated bubbles in fixed beds

To investigate the dynamics of isolated bubbles moving in a fixed bed, and in particular their size, shape and velocity, it is worthwhile to identify the relevant dimensionless parameters in order to precisely control the experimental conditions. Among the physical properties, the surface tension σ is retained. For small to moderate absolute pressure levels, the gas density ρ_G, and dynamic viscosity μ_G are much smaller than their liquid counterparts ρ_L and μ_L: thus, assuming an asymptotic regime, they disappear from the analysis. The bed geometry is assumed simple enough to be characterized only by the porosity ε, and the bead diameter d_p (or equivalently by a pore size δ). In particular, inhomogeneities in the packed-bed structure are not considered here. The pore size δ was defined as the diameter $\delta = d_p(2/\sqrt{3} - 1)$ of the inscribed circle in the space formed by three touching spheres: this area is representative of the cross-section available for bubbles in the selected bed structure (Figure 4).

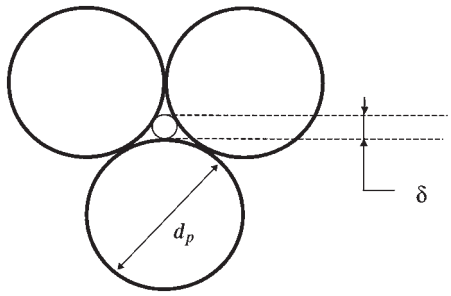

Figure 4. Definition of the characteristic pore dimension δ.

The external vessel dimension D_c is supposed to be large enough to be compared with the bead diameter d_p, and, thus, it does not enter the list of relevant physical parameters. Ones also requires the liquid superficial velocity V_{SL}, a typical bubble size $d = 2a$, and the gravity g. Thus, five independent dimensionless numbers characterize that situation. Introducing the capillary length $a_c = (\sigma/\rho_L g)^{1/2}$, a possible set is the following: the porosity ε, the pore-size scaled by the capillary length δ/a_c, the Morton number $Mo = g\mu_L^4/(\rho_L^2\sigma^3)$ that characterizes the two fluids, the bubble size relative to the pore size a/δ (or a/a_c, which is a Bond number), the Capillary number $Ca = \mu_L(V_{SL}/\varepsilon)/\sigma$. Instead of Ca, one can also use the liquid Reynolds number $Re_L = \rho_L V_{SL} d_p/(\mu_L(1 - \varepsilon))$. In principle, all the unknowns, such as the bubble shape, velocity should be a function of these five groups. It must be stressed that the bubble size is not known *a priori* (unless the bubble size at injection remain smaller than δ, as we shall see later). Extending the earlier analysis to a two-phase flow in a fixed bed, one also needs to consider the gas superficial velocity V_{SG}, and a new dimensionless parameter enters the problem, namely the gas flow rate fraction β already defined. In addition, one may also add some parameters representative of the actual-size distribution (such as various moments).

Experimental setup and measuring techniques

The experiments were performed in a 50 cm long tube with a 30 mm by 30 mm square cross section (Figure 5), filled with glass spheres uniform in size (say within 10%). Different glass beads were considered, with a diameter ranging from 2 to 6 mm: the resulting arrangements were nearly rhombohedric, with an actual porosity evolving between 38 and 41%. The packed bed was maintained fixed between two grids, so that the fluid velocity, directed against gravity, can be changed at will. The later was controlled by way of a pump equipped with a frequency modulator to minimize calorific losses. Optical access has been made possible over the whole column by matching the refractive index of the solid particles constituting the bed with that of the surrounding liquid. A monochromatic (wavelength 589 nm), 400 W, low-pressure sodium lamp was employed for the index matching experiments. Using backlightning, the bubbles travelling in the core of the porous

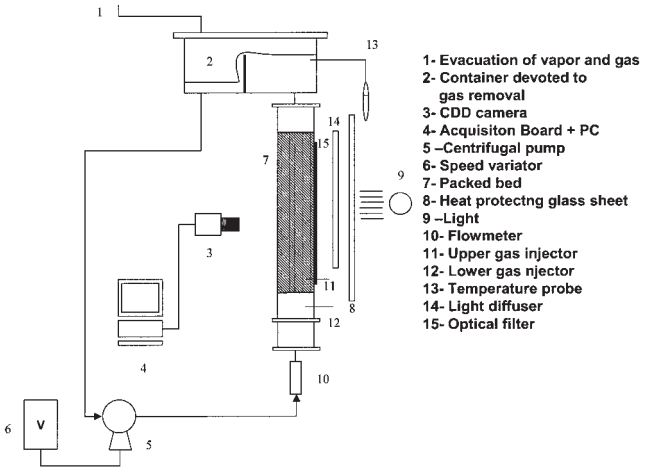

Figure 5. Experimental apparatus.

medium were then easily captured by a 8 bit CCD camera (Figure 5).

The gas was injected through a needle located either below the first grid or inside the bottom part of the bed. The bubble size at injection was systematically quantified, and it was always much larger than δ. A transparent porous medium was quite convenient for the control of the experimental conditions. In particular, all the data presented, hereafter, correspond to bubbles located in the core of the packed bed, so that both the size distribution and the relative velocity measurements were not influenced by the walls of the vessel. The image processing, performed using the Scion Image and Matlab softwares, consisted of the following steps: background substraction, noise elimination, computation of the local gradients, thresholding these gradients and bubble identification, which finally lead to the bubble size and shape. The equivalent diameter of the bubbles was taken as the diameter of the sphere having the same projected area. The ratio between the long and the short axes was also extracted to estimate the bubble deformation.

The selected magnification, which was at least 15 μm/pixel, enables the detection of objects about 30 μm. Such a resolution is well adapted since the smallest bubbles detected were about 80 μm in diameter. Note that the magnification was estimated from the image of the glass beads located in the focus plane: these beads are well calibrated (for instance, the diameter of the 2.45 mm beads was 2450 μm $\pm$ 50 μm) so that the resulting uncertainty is less than 2%. The sensitivity of the size measurements with regard to the lightning conditions, and the threshold selection has also been carefully analyzed. Criteria were simultaneously applied on the grey level and on its gradient. First, blurred, out of focus bubbles were eliminated. The thresholding was then applied on grey-scale gradient, and the size was found weakly sensitive to the threshold detection. Accounting for all these error sources, the relative uncertainty on the bubble size was less than 10% for bubbles above 400 μ, and up to 15% for the smallest bubbles detected.

This nonintrusive technique has also been exploited for velocity measurements using standard and high speed cameras (see third section).

In order to investigate the influence of viscosity and surface tension on the bubble dynamics, several liquids were tested those physical properties are listed in Table 2. These liquid are water, cyclooctene and a product of the Cargille manufacturer (Cargille Code 5095). This later fluid will be denoted Liquid A in this article. As the liquid refractive index evolves with its viscosity (cf. Table 2), different types of glass beads were used to ensure the index matching. With liquid A, glass beads from Fisher Scientific (ref A25080226-242-267) were employed, while Duran borosilicate glass beads from Work Glaskugeln Gmbh (ref 1030805) have been used with Cyclooctene. These beads exhibit a very narrow-size distribution (deviations from the mean diameter are about a few percent), and have a smooth surface.

The influence of the bed geometry, and especially the pore size, on the bubble-size distribution, was also scrutinized.

The hydrodynamic conditions covered a large range of liquid superficial velocities. Yet, they were restricted to low gas fractions because of the limitation of the visualization technique which becomes poorly effective for β above about 2%. Moreover, large gas bubbles can remain trapped in the core of the bed (see for example 28): such situations have been avoided

Table 2. Liquid Properties—Kinematic Viscosity ν_L, Density ρ_L, Refractive Index n_D, Surface Tension σ; Bed Geometry—Bead Diameter d_p and Interstice Dimension δ; and Accessible Range in Terms of Liquid Reynolds Number, Gas Flow Rate Fraction β, and Capillary Number

Liquid	Properties	Bed Geometry: Beads and Pore Size	Mo	Re_L	β	a_c, mm	a_c/δ	Ca
Cargille code 5095 (Liquid A)	T° = 25°C ν_L = 13 10^{-06} m^2/s ρ_L = 899 kg/m^3 μ_L = 11.7 mPa · s σ = 31 mN/m n_D = 1.52	d_p = 2 mm, δ = 309 μm d_p = 4 mm, δ = 618 μm d_p = 6 mm, δ = 927 μm	6.8 10^{-06}	8–64	$\ll$1%	1.87	6 3 2	0.032–0.085
Cyclooctene	T° = 20°C ν_L = 1.42 10^{-06} m^2/s ρ_L = 848 kg/m^3 μ_L = 1.21 mPa · s σ = 32.9 mN/m n_D = 1.46	d_p = 2.45 mm, δ = 379 μm d_p = 5 mm, δ = 772.5 μm	6.96 10^{-10}	102–629	<2%	1.98	5 2.5	0.0035–0.011
Water	T° = 20°C ν_L = 1.0 10^{-06} m^2/s ρ_L = 1000 kg/m^3 μ_L = 1 mPa · s σ = 72 mN/m	d_p = 2 mm, δ = 309 μm	2.6 10^{-11}	270–400	$\ll$1%	2.7	8	0.0031–0.004

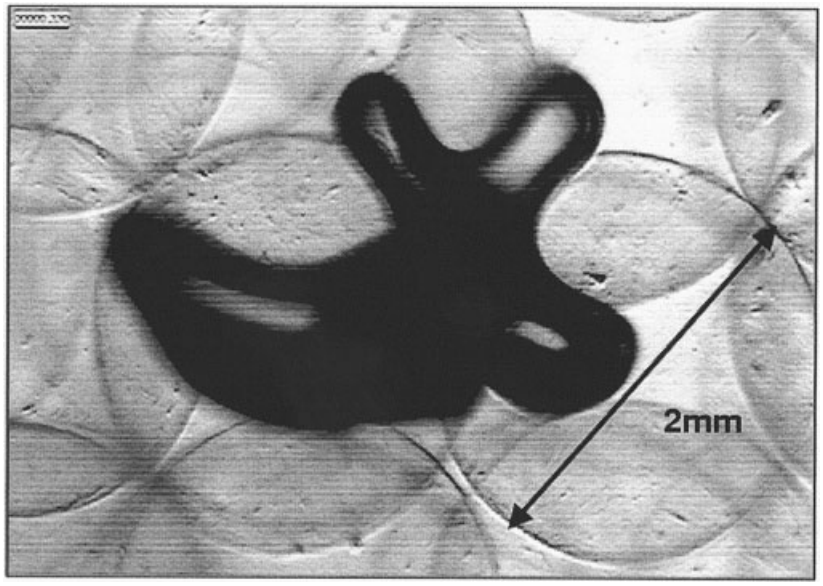

Figure 6. Bubble visualization using index matching.

by setting a minimum liquid velocity, those value depends on the liquid and on the bead diameter. The conditions covered in the experiments are summarized in Table 2. It is worth underlying that, in all these experiments, the capillary length a_c was significantly larger (factor 2 to 8) than the pore size δ. An example of the picture is given in Figure 6.

Bubble-size distribution

When flowing through a fixed bed, bubbles are undergoing stresses, which tend to deform them and can eventually lead to breakup, depending on the bubble size and the local flow conditions. An example of such a breakup event is presented in Figure 7a. The index matching technique allows to trace the evolution of the bubble-size distribution with the height z above the bottom grid. Such an evolution is illustrated in Figure 7b where the bubble diameter has been scaled by δ (on that figure, the bead diameter is $d_p = 2$ mm, which corresponds to $\delta = 309$ μm). For that test, the bubble size at the injection was large, of the order of 6 δ. As the bubbles travel up in the bed, the largest size classes are progressively depleted. Indeed, these inclusions, which are either too large to keep moving through the bed or too slow, break into smaller globules, which may themselves break into even smaller bubbles. For a distance z above about 20 cm, which corresponds to about 80 beads layers, the size distribution no longer evolves, indicating that a frozen state has been reached, or equivalently that the fragmentation process has stopped.

Interestingly, the bubble-size distribution at steady state is not that large: the diameters range from about 100 μm (0.3 δ), up to 900 μm (3 δ). The bubble population is, therefore, a mix between tiny bubbles, smaller than the characteristic pore size, a significant proportion of bubble of the order of the pore size and a few bubbles larger than δ.

The distance required to reach the frozen state is a useful parameter for operating packed-beds reactors. A more significant parameter is probably the number of beads layers a bubble has to cross before the breakup process stops. That variable depends on the initial-bubble size, in addition of flow conditions. For initial bubbles in the range 3–10 δ, the experiments have demonstrated that 30 up to 80 beads layers are required to

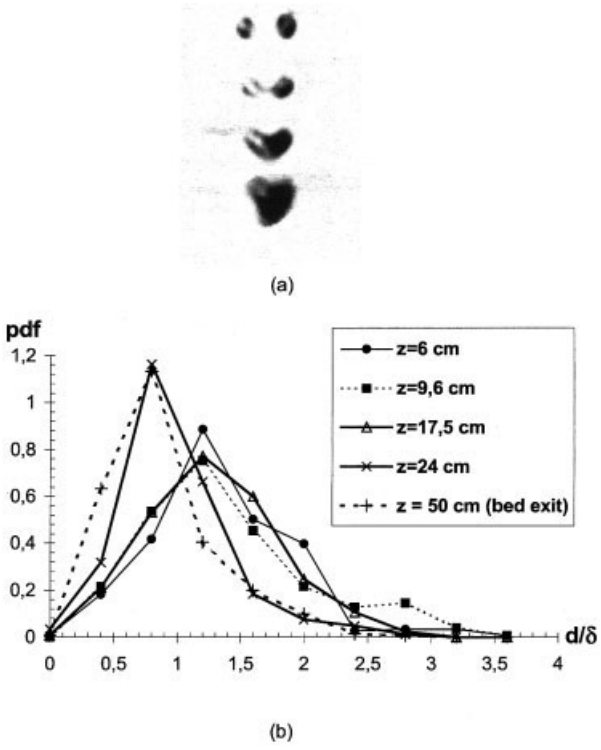

Figure 7. (a) Typical breakup event giving birth to two daughter bubbles. (b) Evolution of the bubble-size distribution as a function of the penetration distance *z* in the bed.

Cyclooctene; $V_{SL} = 6.3$ cm/s; $d_p = 2$ mm; $\varepsilon = 0.38$, $Re_L = 178$; $\beta = 0.12\%$; Bubble diameter at injection about 6δ.

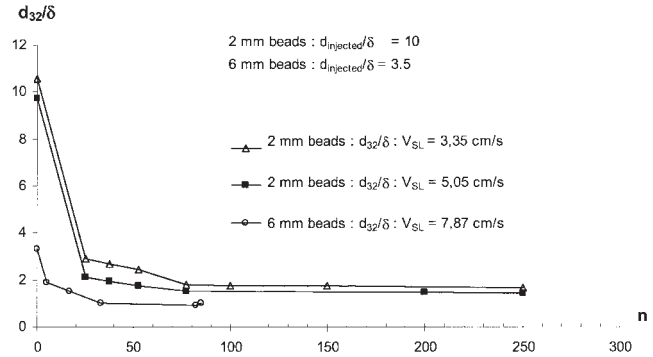

Figure 8. Length required to reach the frozen state.

reach the frozen state, as shown by the evolution of the Sauter-mean diameter with the distance from injection (Figure 8).

The breakup dynamics will not be further analyzed here. Instead, let us focus on the sensitivity of the frozen bubble-size distribution to operating conditions. The size measurements have been performed near the bed exit, just below the upper grid. For water, as there is no visual access inside the bed, the images were taken just after the upper grid (its mesh size was large enough, above 1.8 mm, to avoid any alteration of the size distribution). First, the liquid velocity has been changed for a given liquid and a given bed geometry. As shown in Figure 9a, the bubble-size distribution proves to be nearly the same, although the velocity has been multiplied by 1.5 (one can notice a slight decrease in the proportion of large bubbles for the highest liquid velocity, indicating perhaps a more efficient breakup process). To check the influence of the physical properties, and enlarge the accessible range in terms of Re_L, the experiment was repeated in the same bed for various fluids and liquid velocities. As shown in Figure 9b, the size distribution is nearly unaffected although the liquid viscosity has been varied by a factor 13, the surface tension by a factor 2 and the velocity by a factor 2. These results unambiguously demonstrate that a liquid Reynolds number evolving between 16 to 400 has no influence on the frozen-size distribution. In addition, the surface tension has no effect, at least for Capillary numbers in the range $4\ 10^{-3}$ to $6\ 10^{-2}$.

So far the bed geometry has been kept fixed. In order to demonstrate its key role, size distribution measurements were performed for beads of different diameters. As shown in Figure 10a, the corresponding frozen-size distributions almost superpose with each other although the pore size δ has been varied by a factor 3. In addition (1) the peak in the bubble-size distribution remains of the order of the pore characteristic dimension δ, and (2) the observed minimum and maximum bubble size (respectively, about 300 μm and 3,000 μm) corresponds to the limits 0.2–0.3 δ, and about 3 δ, already observed in the experiments with the 2 mm beads. This is the clear mark that the bed geometry alone controls the bubble size at steady state.

The earlier results have been obtained at low gas flow rate fractions, say for β below 0.1%. When the gas fraction increases, one may wonder whether the size distribution is altered, or even whether a frozen state is still present. Indeed, hydrodynamic interactions between bubbles, as well as flow redistribution mechanisms between adjacent pores may promote coalescence. Yet, the result is difficult to anticipate since on the one hand, the bubbles trajectories are strongly constrained by the presence of the solid beads, and on another hand, preferential paths could appear. To address this point, some measurements have been performed until the imaging technique loses its efficiency, that is up to β about 2%. In that range, and as illustrated by Figure 10b, the size distribution is nearly insensitive to β.

The bubble shape at equilibrium has been examined by way of an eccentricity e defined as the ratio of the longest to the shortest chords defined on the bubble projected area.

The Figure 11, which provides e as a function of d/δ for a specific experiment, shows that the bubble deformation remains moderate ($e < 1.5$) for bubble diameters up to about 1.3 δ. Much stronger distortions, up to $e = 2.5$, arise only for bubbles larger than 1.5 δ, and, thus, concern but a small proportion of the gas inclusions.

The experiments presented in that section have shown that, provided that the liquid velocity is large enough to avoid the blockage of bubbles in the porous matrix, the bubble-size distribution reaches a steady state before about 80 bead layers

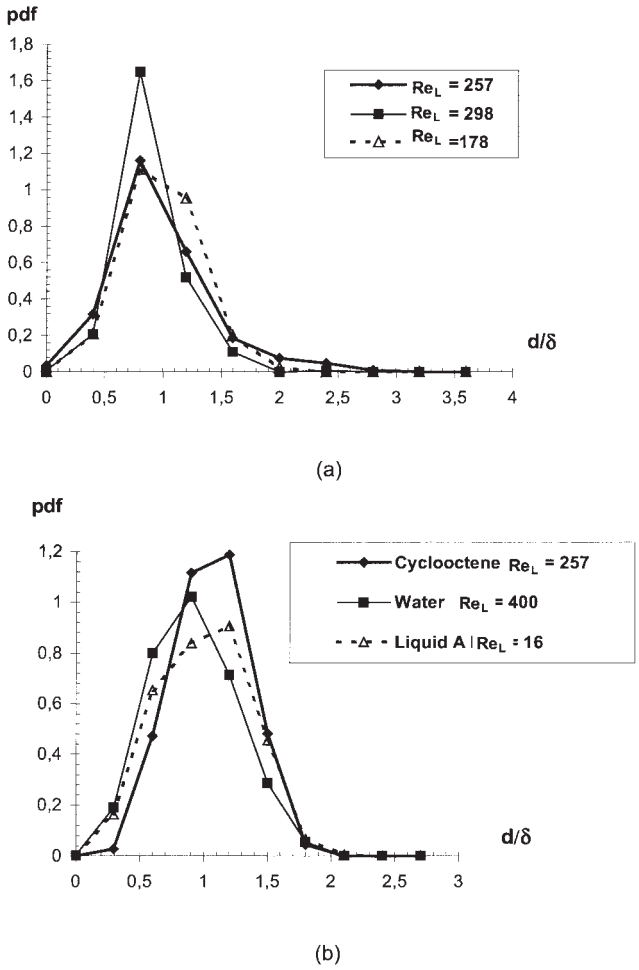

Figure 9. (a) Effect of Re_L on the bubble size distribution at equilibrium.

Cyclooctene, $d_p = 2.45$ mm. (b) Effect of the physical properties on the bubble-size distribution at equilibrium Cyclooctene, $d_p = 2.45$ mm, $V_{SL} = 9.1$ cm/s, water: $d_p = 2$ mm, $V_{SL} = 12$ cm/s; liquid A: $d_p = 2$ mm, $V_{SL} = 6.3$ cm/s, $\varepsilon = 0.38$.

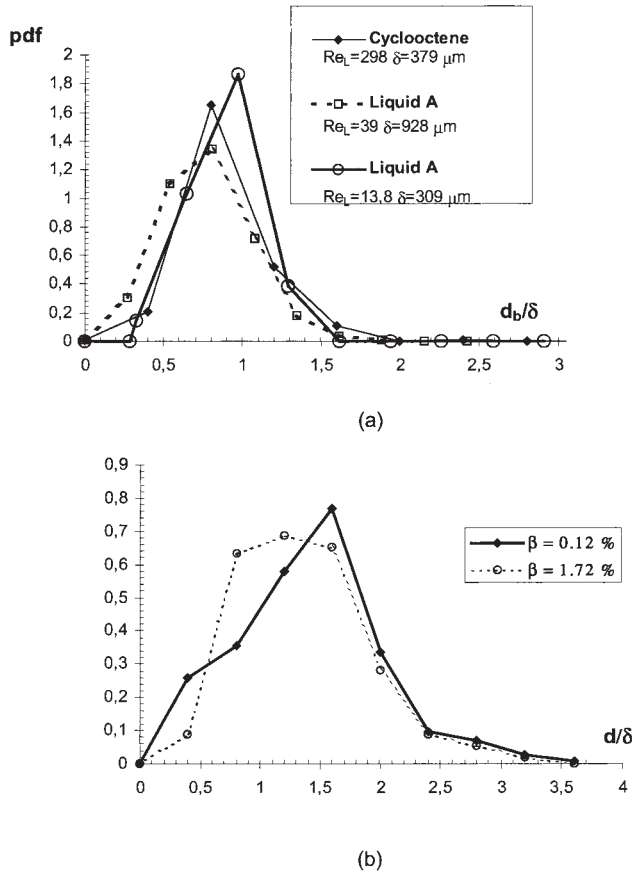

Figure 10. (a) Effect of the pore size δ on the bubble-size distribution. (b) Effect of β on the bubble-size distribution.

from the injection. Moreover, that frozen distribution is primarily controlled by the bed geometry. The recorded sizes are consistently comprised between 0.2–0.3 δ and 2 to 3 δ. The arithmetic bubble dia. d_{10} is about 1.1 δ, the d_{30} is about 1.4 δ^3 and the Sauter-mean dia. d_{32} is about 1.2 δ. Of course, such scales are valid for bubbles that have experienced a breakup process (that is, for bubble size at injection exceeding δ, and for large distances from the injection).

These results significantly ease the modeling of bubbly flows in packed beds. First, the existence of a frozen-size distribution implies that breakup and coalescence processes need not be considered (at least, over a moderate range of variation of the absolute pressure). Second, as the bubble-size distribution only depends on the packed bed geometry, no closure law is required to account for a possible influence of the flow conditions on these quantities. Hence, these findings support the model proposed in the first section, and based on a single equivalent bubble diameter. Let us also note in passing that the interfacial area density can, therefore, be estimated using the classical expression $6\alpha/d_{32}$ once the void fraction is available. In addition, more sophisticated modeling approaches are also feasible since the frozen-size distribution can be well approximated by the following normal distribution:

$$P(d/\delta) = \frac{1}{s\sqrt{2\pi}} \exp\left(-\frac{[d/\delta - m]^2}{2s}\right) \tag{36}$$

with $m = 1.1$ and $s = 0.27$. All the earlier reported behaviors are expected to remain valid while the pore dimension δ does not exceed the capillary length. Yet, their range of validity in terms of gas flow rate fraction is not precisely known. Indeed, as β increases, and before the disappearance of the dispersed regime, one may expect the occurrence of preferential paths for the gas inducing spatial inhomogeneities and possibly strong distortions in the bubble-size distribution. Within these restrictions, we are now in position to supplement the proposed model with the lacking information, namely the closures for the mesoscale relative velocity U_r, and for the liquid-solid force density f_{LS} on the basis of phenomena arising at the microscale.

Closure Proposals

Relative velocity at mesoscale

No data is available about the relative velocity at mesoscale. Yet, it has just been shown that most bubbles have a size of the order of the pore dimension, and we expect them to behave similarly as large slugs subject to a forced flow. Thus, their relative velocity should be proportional to the mean-liquid velocity (see, for example,[29–32]). To test this assumption, two approaches have been exploited. First, the velocity of isolated bubbles has been directly measured in cocurrent upflow. Second, the kinematic Eq. 34 has been used to evaluate the relative velocity at mesoscale using available experimental data gathered in various conditions.

Beforehand, a reliable measuring technique has to be defined for the mesoscale average-relative velocity. For that purpose, the case of an isolated inclusion in a fixed bed has been considered. Such a bubble is expected to undergo successive accelerations and decelerations due to its passage in narrow and wider interstices. These expectations are confirmed by the time evolution of the bubble velocity presented in Figure 12. The later happens to be pseudoperiodical, the pseudo-period being equal to one bead diameter. Moreover, the bubble velocity experiences large variations that exceed by far its time average, the later being here about 4 mm/s. This average is representative of the mesoscale averaging introduced in the first section. More precisely, the z component of the average bubble velocity at mesoscale $U_b = \langle u \rangle$ is directly accessible by considering the time required for a bubble to travel a vertical distance that is

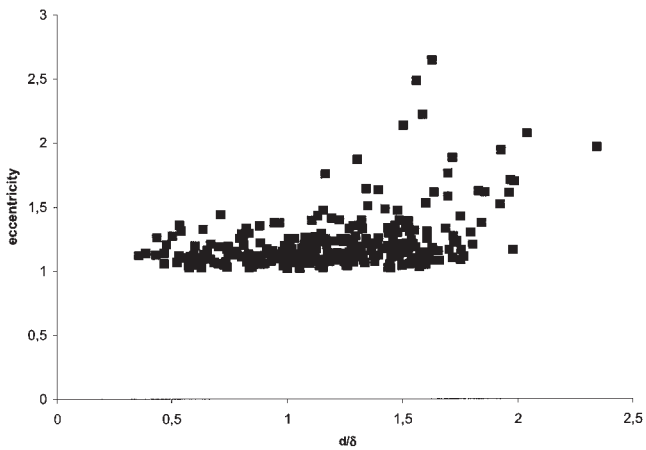

Figure 11. Eccentricity e vs. d/δ. Liquid A. d_p = 2 mm. V_{SL} = 3.1 cm/s. 268 bubbles in the sample.

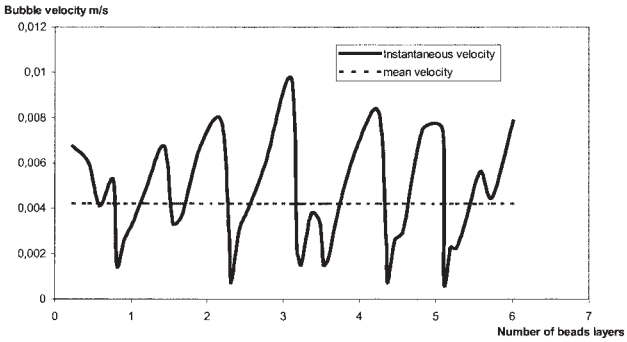

Figure 12. Measurement of the instantaneous bubble velocity. Cyclooctene, d_p = 2.45 mm, V_{SL} = 0, bubble dia. 285 μm, that is, d/δ = 0.75.

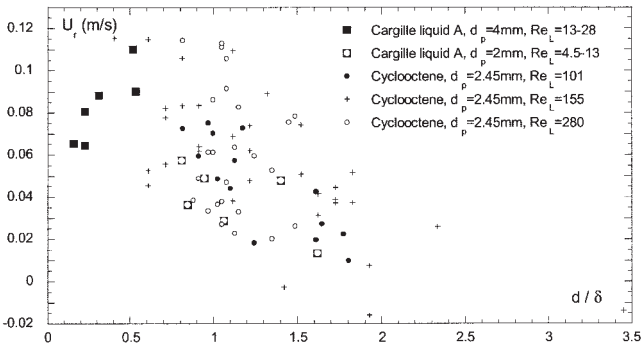

Figure 13. Average relative velocity of isolated bubbles in packed beds (ε = 0.38 in all conditions).

large compared with the bead size. Next, in order to evaluate the mesoscale relative velocity between the phases, the mesoscale axial velocity in the liquid $\langle v \rangle$ is needed. Direct measurements of the liquid velocity field inside the packed beds were not attempted. Instead, we rely on Ogawa et al. experiments[33] in single phase flow, who succeeded to collect by an NMR technique the velocity pdf over a significant volume. Their data demonstrate that the axial velocity averaged at mesoscale is very close to the average axial liquid velocity V_{pore} in the interstices as given by

$$V_{pore} = \frac{V_{SL}}{\varepsilon} \tag{37}$$

Hence, the "apparent" relative velocity of the bubble U_{rapp} defined as

$$U_{rapp} = U_b - V_{pore} \tag{38}$$

happens to be identical to the mesoscale average relative velocity of the bubble U_r that enters Eq. 34. Let us underline that the expected deviations between U_r and U_{rapp} are those due to the difference between the quantities $\langle v \rangle$ and V_{pore}: the later may possibly become significant in two-phase flow conditions. In absence of contradictory experimental evidence, it will be considered that $\langle v \rangle = V_{pore}$.

On that basis, U_r has been measured for various bubble sizes. The later was controlled using different injection needles and thanks to a careful adjustment of the gas flow rate. To investigate the influence of the flow conditions, the experiments have been performed for two liquids, for different pore size and for various liquid flow rates. The evolution of U_r with the dimensionless bubble size d/δ is given in Figure 13. Owing to the limited number of data, and the fact that they correspond to variable flow conditions, it is difficult to identify from this plot what is the part of the relative velocity due to the action of gravity (the later is small but not zero as shown in Figure 12). Various interesting features can nevertheless be identified. First, U_r increases with the bubble size provided that the later is significantly smaller than δ. More precisely, for $d/\delta < 0.5$, $U_{rapp} \propto d^{0.29}$, which is a much weaker dependency than the d^2 behavior of the terminal velocity in unconfined medium, as well as in moderately confined situations (such as for the creeping motion of a spherical bubble in a capillary tube those size is a significant fraction of the tube diameter analyzed by 12). The confinement alone cannot explain these observations, and the interface deformation is expected to play a key role. This is further confirmed by the behavior of large bubbles. For sizes exceeding 0.5–0.7δ, the relative velocity decreases with the size, as $U_{rapp} \propto d^{-1.25}$. In addition, U_r tends to zero for diameters in the range 2–3δ (the negative values in Figure 13 are due to measurement uncertainty): this is physically consistent because such large bubbles experience very strong deformations when crawling from one bead layer to the next one. As expected, and contrary to Attou et al. assumptions, the average velocity of isolated bubbles in a packed bed is not captured by the correlations established in an infinite medium. In addition, these results emphasize the distinct behaviors of the various size classes so that, following the discussion in the section "*Exploitation of the balance equations at mesoscale,*" the evaluation of the momentum transfer in such two-phase flows is by no means straightforward. A comparison of the experimental results with the available studies concerning the dynamics of long slugs in rectilinear capillaries is relevant. The later indicate that the bubble velocity U_b evolves in proportion to the mean liquid velocity $\langle v \rangle$, and also that the ratio $U_b/\langle v \rangle$ should increase with the Capillary number (see, for example,[29,31,34,35]). To test this, the data of Figure 13 have been replotted as U_r/V_{pore} vs. d/δ. Although limited, these results indicate that U_r/V_{pore} is of order unity, which supports the fact that the relative velocity is mainly controlled by the mean liquid flow. Besides, U_r/V_{pore} is marginally sensitive to V_{LS}, and, thus, to Ca (in Figure 14, Ca evolves between 4 10^{-3} and 7 10^{-2}). It is known that the

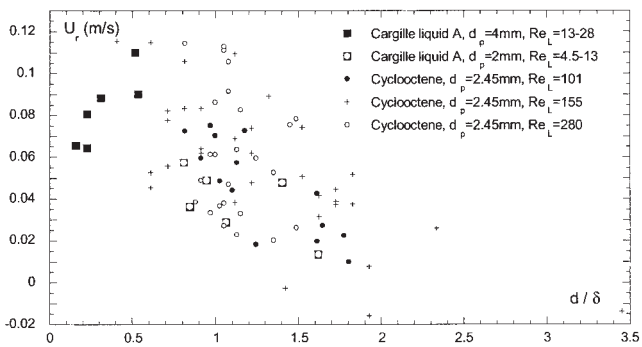

Figure 14. U_r/V_{pore} vs. d/δ for isolated bubbles.

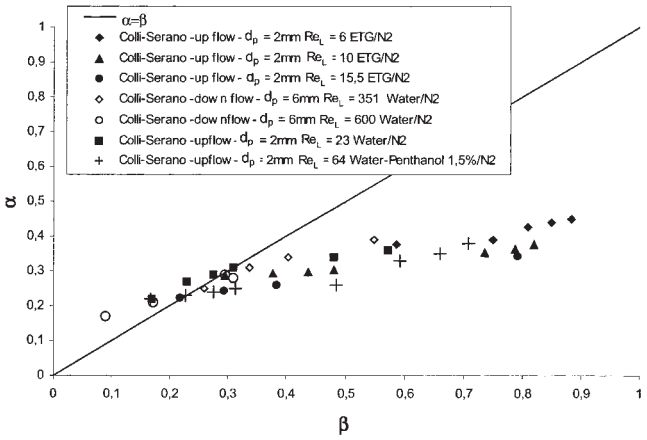

Figure 15. α vs. β. Colli-Serano data.

dynamics of a slug in a straight capillary is strongly dependent on the flow organization around the gas inclusion, and in particular, on the interface deformation and on the resulting structure of the liquid film (which provides the Ca dependency). In packed beds, the situation is quite different because the neighboring pores can be freely used as a bypass. Moreover, the hydraulic diameter of these bypass is fixed by the bed geometry. These features probably explain the weak sensitivity of U_r/V_{pore} to the capillary number in packed beds. More refined investigations would be useful to quantify this sensitivity.

To gain some insight in the relative velocity for finite void fractions, and to test further the role of the carrier flow, the relationship (Eq. 34) has been exploited in conjunction with reliable experimental data. For all these data, it has been checked that the measurements were achieved beyond the 100 beads layers limit above the injection. It is, therefore, expected that they are all associated with frozen bubble bubble-size distributions. Figure 15, which gives the evolution of the void fraction α vs. β according to the experiments of Colli Serano,[36] provides some key information. First, for $\beta > 0.2$, the void fraction happens to be less than β irrespectively of the flow direction compared with gravity. According to Eq. 34, that feature indicates that the relative velocity is always positive along the flow direction: this is in agreement with a slug dynamics those velocity exceeds the mean-liquid velocity. Moreover, the role of gravity on the relative velocity happens to be either not relevant or negligible. Second, all the data of Figure 15 almost collapse on the same curve whatever the liquid Reynolds number. Therefore, the ratio U_r/V_{pore} that enters the Eq. 34 does not evolve with V_{SL}, in agreement with the observations made on isolated bubbles. Let us note that the absence of liquid Reynolds number dependency of the results presented in Figures 15 and 16 can be seen as an indirect confirmation that a "frozen" state in terms of bubble size was indeed reached for all the flow conditions considered.

Furthermore, all these elements suggest that the bubbles in a packed bed behave as long slugs, and that the mesoscale relative velocity can be expressed as

$$U_r = (C - 1)V_{SL}/\varepsilon \tag{39}$$

where the contribution of gravity to the relative velocity has been neglected, and where the coefficient C evolves with flow conditions. Let us recall that for isolated slugs in large tubes, C typically varies between 1 up to more than 2.[29,37]

Using the kinematical relationship (Eq. 34), the ratio U_r/V_{pore} has been extracted from the data of Colli Serano. Such an approach provides a relative velocity for the bubble cloud, that is, it cannot distinguish between the various size classes. As shown in Figure 16, U_r/V_{pore}, and, thus, C happens to be a unique function of the gas flow rate fraction. In particular, C does not depend on the liquid superficial velocity. According to Figure 16, a sharp transition arises at β about 0.7, which corresponds to the onset of the trickle bed regime. Below β about 0.6–0.7, C is almost linearly increasing with β. Interestingly, C is comprised between 1 and 4, a magnitude that remains comparable with the values identified for two-phase slug flows in ducts. The increase of the relative velocity with β is a key feature of two-phase flows in fixed beds. That behavior can be tentatively attributed to collective effects, and more precisely to the formation of preferential gas paths inside the bed (eventually in conjunction with an evolution of the bubble-size distribution). These considerations are valid for β above 0.15–0.2. For lower gas contents, the interpretation of Figure 16 is much more delicate. Indeed, according to the Eq. 34, the quantity $(\alpha - \beta)/\alpha$ required to evaluate U_r becomes extremely sensitive to the measurement uncertainty on α while the measuring techniques are poorly sensitive at low-void fractions. Moreover, and especially at low-liquid velocities, some bubbles can be trapped in the packed bed and, thus, can induce a significant error on the void fraction associated with mobile bubbles. All these shortcomings preclude any reliable interpretation of the data gathered at $\beta < 0.15$–0.2. In particular, the examination of the data of Figure 16 for $Re_L = 600$ in downflow conditions indicate that $\alpha > \beta$. Moreover, they imply a strong relative velocity: at $\beta = 0.09$, U_r should equal -8 cm/s while $V_{SL} = 5$ cm/s. Such results seem hardly physically consistent, even if ones invokes the formation of preferential paths that would allow the gas to flow up at large speeds under the action of gravity. Thus, in the range 0.15–$0.2 < \beta < 0.6$–0.7, the coefficient C entering Eq. 39 happens to be linear in β, so that the relative velocity writes:

$$\varepsilon U_r/V_{SL} = K\beta + C_0 \tag{40}$$

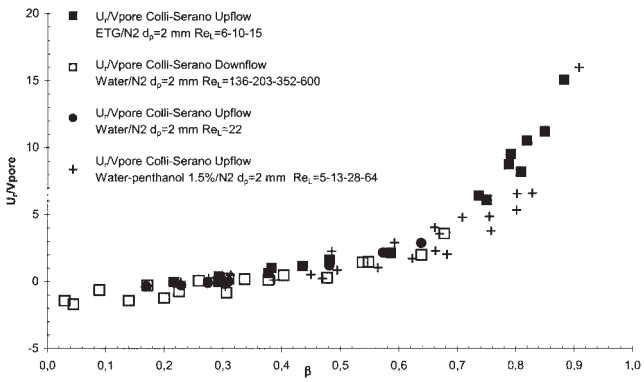

Figure 16. U_r/V_{pore} vs. β. Colli-Serano data.

A linear fit of the data presented in Figure 16 provides $K \sim 6.7$ and $C_0 \sim -1.9$. The data and their analysis presented here confirm our expectation that the bubbles in a fixed bed behave similarly as slugs in ducts. Strong differences were nevertheless identified. In particular, the proportionality coefficient between the bubble-relative velocity, and the liquid-mean velocity is a unique function of the gas content and does not evolve significantly with the liquid flow conditions. The resulting closure for U_r as given by Eq. 40 need to be checked more thoroughly. In particular, some questions remain concerning the behavior of the relative velocity when the gas phase fraction is less than about 0.2. These questions will be addressed in a companion article.

Liquid-solid friction in two-phase flows

Previous proposals concerning the liquid-solid interaction term, f_{LS} have been recalled in the introduction. That of Benkrid et al.[8] accounted for an increased porosity, and that of Attou et al.[1] accounted also for the liquid residence time. These proposals do not take into account the dynamics of bubbly flows at small scale. Thus, information available at the pore scale has been analyzed in order to propose a more relevant closure.

Idealized model of the two-phase pressure drop

The liquid-solid interaction term f_{LS} arises from the viscous friction on the surface of the solid beads, but also from localized pressure drops induced by the presence of bubbles in the pores. Indeed, recalling that the average bubble size has been found of the order of δ, most of the bubbles present in the fixed bed are similar to slugs at the pore scale. Compared with a pure liquid flow, two modifications are therefore expected. First, for wetting liquids, the passage of a bubble in a tube leaves a small liquid film on the solid[38,39] those thickness h increases as $Ca^{2/3}$ in the limit of small capillary numbers (such a scaling is probably not applicable in fixed beds because of the bypass phenomena evoked in the section "*Relative velocity at mesoscale*"). Along the bubble length, the viscous stress on the solid is expected to scale as $\mu_L V/h$, where the reference liquid velocity V is of the order of the bubble velocity. Since the later equals or exceeds the liquid intersticial velocity V_{SL}/ε, one expects an increase of the local viscous stress on the solid any time a bubble is located in its vicinity. This mechanism leads to an increase of the viscous friction in proportion of the bubble number density, or equivalently of the void fraction. The second and main effect related with the passage of a long bubble—long at the pore-scale—is the apparition of an extra pressure drop related with normal stress jumps at the front and at the rear of the inclusion. This "singular" pressure drop Δp_s originates from the capillary excess pressure, those magnitude is given by the surface tension over the local interface curvature that is of the order of δ for interstices smaller than the capillary length. Its precise contribution depends on the local flow structure which itself depends on the tube geometry, and can be coupled with surfactants dynamics. Available studies have been mainly devoted to elongated bubbles in rectilinear capillary ducts. They demonstrate that, for a tube of radius R, the quantity $\Delta p_s/(\sigma/R)$ increases with the Capillary number $Ca = \mu_L \bar{V}_L/\sigma$. For example, the numerical simulations of an axisymetrical clean bubble by 40 provide the following behavior

$$\frac{\Delta p_s}{\sigma/R} = 4.52(3 \cdot Ca)^{2/3} - 12Ca^{0.95} \quad (41)$$

valid for Ca up to 0.1. The first term in the r.h.s. of the equation is the analytical result established by[38] in the limit of vanishing Ca. Similar behaviors are reported for various geometries[41] including angular capillary tubes such as squares[42] or even more complex shapes indicating that the trends of Eq. 41 are weakly sensitive to the channel geometry. A key feature of Eq. 41 is that the pressure drop does not depend on the bubble size. In addition, and concerning the influence of surfactants, it is worth mentioning that, contrary to liquid-liquid systems,[43] gas-liquid flows seem to be poorly sensitive to surfactants.[41] In a fixed bed, the situation is more complex since the bubble shape is evolving when passing from one bed layer to the other one. Yet, the pressure jumps Δp_s are still present, and one expects the Ca number to control the dynamics even if the flow can bypass the bubble by way of a neighboring interstice. The key role of the parameter Ca on the pressure is a marked difference with the behavior of the bubble velocity as previously discussed. Based on these results, the singular pressure loss due to a single bubble in the capillary can be written as

$$\Delta p_s = \sigma/\delta Ca^n f_1(geometry, Re_L, surfactants \ldots) \quad (42)$$

where $n < 1$ according to available results.

So far, only moving bubbles have been considered. Yet, depending on flow conditions, some bubbles can be trapped (for a variable duration) in the pores. When it is so, the liquid is redistributed into the adjacent pores, the intersticial velocity increases, and, thus, the friction on the solid matrix is enhanced. That phenomenon is more or less equivalent to consider that the bed porosity has been decreased by an amount proportional to the volume fraction, $\alpha_{blocked}$, of the trapped gas bubbles. ε is, thus, changed into $(1 - \alpha_{blocked})\varepsilon$. As very little is known about $\alpha_{blocked}$, the later will not be taken into account in the sequel; such an assumption seems valid at large liquid velocities. A bubbly flow in a packed bed can be idealized as a set or connected tubes of length L, and radius δ, each filled with N moving bubbles of size $O(\delta)$. The void fraction is, thus, proportional to $N\delta/L$. The total pressure loss can be roughly evaluated as the combination of a regular pressure loss over the length $(L - N2a)$, and the sum of the "singular" pressure losses due to each inclusion as well as of the enhanced friction. Thus

$$\Delta P = C_f \mu \bar{V}_L L(1 - \alpha)/\delta^2 + N\Delta p_s + NC'_f \mu \bar{V}_L/\delta \quad (43)$$

where C_f is a friction coefficient evolving with the geometry, and where the last term accounts for the friction enhancement by bubbles passing nearby the solid matrix. Therefore, the ratio between the pressure drop in that idealized two-phase flow and its counterpart in a single-phase flow at the same liquid velocity writes

$$\frac{f_{ls}}{f_{ls,1\varphi}} = 1 + \alpha[f_2 Ca^{n-1} + f_3 - 1] \quad (44)$$

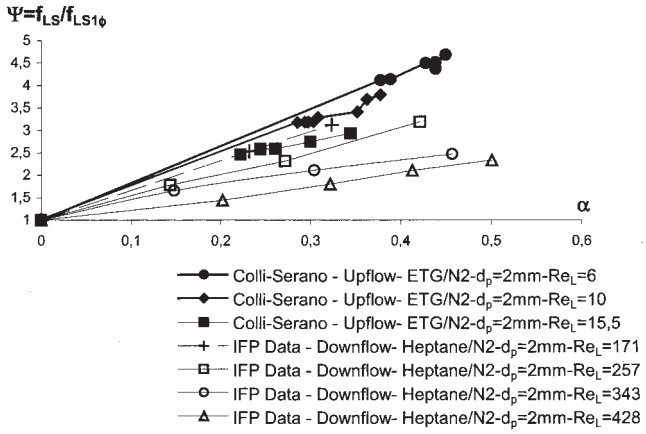

Figure 17. Variation of ψ with α.

where the unknown functions f_2 and f_3 depend on the bed geometry, the flow regime and possibly the presence of surfactants. In a more condensed form, one has

$$\psi = f_{LS}/f_{LS,1\varphi} = (1 + \lambda \cdot \alpha) \tag{45}$$

where $\lambda(Ca, geometry, \ldots)$ is a function to be determined.

The earlier equation suggests a linear evolution of Ψ with α, and a dependency of λ with parameters related with the bubble dynamics at small scale (represented here by the Capillary number). Such a behavior was not anticipated by Attou et al. (see Eq. 5) nor by Benkrid (see Eq. 3). As a first support to the proposed Eq. 45, let us mention that a linear increase of the pressure drop with the gas void fraction is close to what has been observed by[44] for bubbly flows in angular capillaries.

In order to test the consistency of our proposal, we exploited the experimental data from Colli Serano for upflow, and a set of data collected at IFP and presented in Marie-Laure Bordas PhD[45] for downflow. The data have been selected such that all the required information were measured, and such that the behavior of the void fraction vs. the gas flow rate ratio was consistent. In particular, two data sets from Colli Serano have been discarded because α was larger than β. The evolution of Ψ is plotted as a function of α in Figure 17 (*rem:* All the data used for the analysis are not reported on the figure for the sake of clarity). Clearly, the quantity Ψ is linearly increasing with α, as expected from our proposal. Surprisingly, that trend holds up to large gas fractions, close to 50%. In addition, the slopes of these lines evolve with flows conditions (represented here by the liquid Reynolds number). More, for each set of data, namely up and down-flows, the slope is a monotonous function of Re_L (or of V_{LS} since the liquid and the bed geometry are fixed for each set).

To check the expected dependency of the proportionality coefficient with the capillary number, λ has been estimated for the data used for the previous analysis (data of Figure 17 and data of Colli-Serano not plotted on Figure 17). As shown in Figure 18, λ evolves as $Ca^{-0.3}$ which is quite consistent with our closure proposal, and give credit to the role of the microscale phenomena on the pressure drop. Thus, the Eq. 45 combined with the kinematical law (Eq. 34), and its closure law (Eq. 40) constitute a complete system allow to predict the void fraction, and the pressure drop in a granular packed bed for given operating conditions.

Incidentally, the model shows that the closures proposed by Benkrid et al. (Eq. 3), and by Attou et al. (Eq. 5) are not accurate.

Although the physical consistency of our closure proposals has been clearly demonstrated by a comparison with various sets of experimental data (see Figures 15, 16, 17, and 18), that preliminary analysis deserves to be completed by a more thorough examination covering a larger range of flow conditions. To complement our knowledge of the relevant parameters affecting the parameter λ, dedicated measurements were performed at LEGI and IFP. These data were analyzed along with other data sets available in the literature, but, for sake of clarity, this material will be presented in a companion article. Basically its content validates the main conclusions of the present article, both in terms of liquid-gas momentum exchange and in terms of bubble dynamic.

Conclusion

A 1-D Eulerian two-fluid model has been developed for bubbly flows in fixed beds and for wetting liquids. Starting from the local balance equations from the hybrid approach,[16,17,21] their integration over a large volume compared with the small-scale dimensions of the packed bed provide phasic momentum equations at a mesoscale. As for two-phase flows in ducts, these general equations cannot be solved without introducing the dynamics of each phase at small scale. The difficulties are here twofold. First, and contrary to bubbly flows in large vessels, there is no clear scale separation between the dynamics of the continuous phase and of the bubbles. Second, bubbles in a fixed-bed experience strongly unsteady motions, including shape distortion as well as acceleration and deceleration. Such an intricated multiscale problem can, in principle, be solved using direct numerical simulations of the bubble behavior. However, such direct numerical simulations are quite complex and are not yet available for realistic conditions, so that there is presently no way to link the momentum transferred to the liquid phase with the mean force acting on a bubble. Such a statement also demonstrates that the balances earlier proposed by Attou and Ferschneider[1] are incomplete. To overcome that limitation, the mesoscale momentum balance equa-

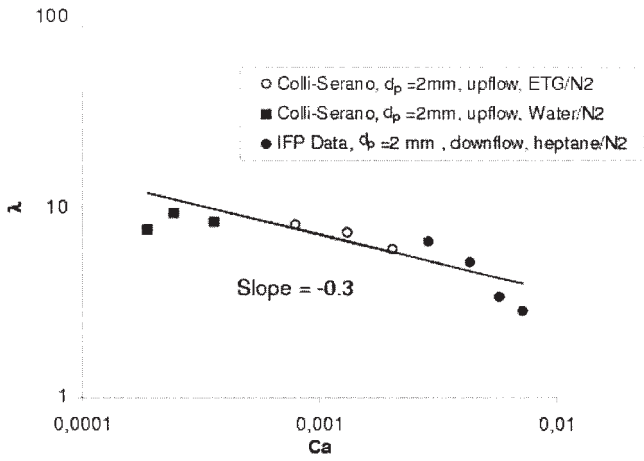

Figure 18. Variation of ψ with Ca.

tion for the gas has not been exploited. Instead, it has been replaced by the kinematic relationship relating the void fraction with the gas flow rate fraction: that relationship requires a closure for the mesoscale relative velocity of the bubbles instead of the average force acting on them. That approach has been justified by the analysis of the bubble-size distribution. Indeed, dedicated experiments have proved that the later is uniquely controlled by the pore scale when the later is smaller than the capillary length scale. Such a result, validated for capillary numbers in the range 10^{-3}–10^{-2}, and in dilute conditions, implies that the bubble size does not pertain to the unknowns. In addition, coalescence and breakup need not to be accounted for (except possibly near the injector). As the bubble size scaled by the characteristics pore size δ evolves in the range 0.2 to 2–3, most bubbles happen to be larger than the hydraulic diameter. It seems then natural to treat them as strongly confined slugs at the pore scale, and thus to postulate that their relative velocity is proportional to the liquid superficial velocity. This assumption proves to be supported by our own experimental investigations performed in the dilute limit, as well as by the analysis of available experimental data from the literature. Yet, and contrary to bubbles confined in a single duct, the relative velocity at mesoscale happens to be weakly dependent on the local flow organization, because the liquid can freely bypass the gas inclusion through neighboring channels: such a flow organization almost eliminates any dependency of the relative velocity with the capillary number. However, the analysis of available experiments indicate that the relative velocity at mesoscale monotonically increases with the gas flow rate fraction. This phenomena is tentatively attributed to the formation of preferential path for the gas: it may explain why the mesoscale relative velocity evolves between 1 up to 4 times the liquid superficial velocity. Concerning the pressure drop in the liquid phase, the later is mainly attributed to capillary excess pressure due to the presence of bubbles those size scales as δ. Consequently, the ratio of two-phase pressure drop to the one-phase pressure drop at the same superficial velocity is expected to linearly increase with the void fraction. In addition, the proportionality coefficient should evolve with the capillary number. These anticipations have been validated using experimental data available in the literature: they demonstrate the role of the bubble dynamics at small scale on the global behavior of two-phase flow in fixed beds.

In this article, the new 1-D model for bubbly flows in packed beds has been proposed that relies on two original closures for the mesoscale relative velocity and the pressure drop. The ability of these proposals to correctly represent the complexity of bubbly flows in fixed beds are encouraging. In addition, they open the way to a more refined analysis of the experimental data. These proposals need to be confirmed over an extended set of flow conditions: new and specific experiments performed at LEGI and IFP will be presented in a companion article. Besides, some open questions remain to be addressed. They notably concern the possible evolution of the bubble size with the gas flow rate fraction, or the role of absolute pressure effects on the bubble expansion possibly leading to some continuous breakup. Another question concerns the fraction of the bubbles that could be trapped in the fixed bed those contribution to the above mentioned closures has not been accounted for. Extensions of the model is required to take into account such a population, those role may become significant at low-liquid flow rates.

Literature Cited

1. Attou A, Ferschneider G. A simple model for pressure drop and liquid holdup in packed bed bubble reactors. *Chem Eng Sci.* 1999;54:5139–5144.
2. De Santos JM, Melli TR, Sciven LE. Mechanics of gas-liquid flow in packed bed contactors. *Ann Rev Fluid Mech.* 1990;23:233–260.
3. Barrios E. *Etude de l'hydrodynamique des réacteurs en lit fixe avec écoulement de gaz et de liquide en co-courant ascendant.* Université Paris VI et ENSPM Paris, France; 1987, PhD thesis.
4. Turpin JL, Huntington RL. Prediction of pressure drop for two-phase, two-component concurrent flow in packed beds. *AIChE J.* 1967;13:1196–1202.
5. Saada MSY. Fluid mechanics of co-current two-phase flow in packed-beds: pressure drop and liquid hold-up studies. *Per Poly Chem Eng.* 1975;19:317–337.
6. Ford LH. *Multiphase flow through porous media, with special reference to the turbulent regime.* University of London, London, UK; 1960, PhD thesis.
7. Ergun S. Fluid flow through packed columns. *Chem Eng Prog.* 1952;48:89–98.
8. Benkrid K, Rode S, Midoux N. Prediction of pressure drop and liquid holdup in trickle-bed reactors operated in high interaction regimes. *Chem Eng Sci.* 1997;52:4021–4032.
9. Macdonald IF, El-Sayed MS, Dullien FAL. Flow through porous media—the ergun equation revisited. *Ind Eng Chem Fund.* 1979;18:199–207.
10. Hinze JO. The flow field in and around a droplet moving axially in a tube. *AIChE J.* 1955;1:289.
11. Ishh M. *Thermo Fluid Dynamic Theory of Two-Phase Flow*. Eyrolles, Paris; 1975.
12. Hetsroni G, Haber S, Wacholder E. The flow field in and around a droplet moving axially in a tube. *J Fluid Mech.* 1970;41:689–705.
13. Ishh M, Mishima K. Study of two-fluids model and interfacial area. *Argone National Library Report ANL-80-111;* 1980.
14. Olbricht WL. Pore-scale prototypes of multiphase flow in porous media. *Ann Rev Fluid Mech.* 1996;28:187–213.
15. Patel PD, Shaqfeh ESG, Butler JE, Cristini VC, Blawzdziewicz J, Loewenberberg M. Drop breakup in the flow through fixed fiber beds: an experimental and computational investigation. *Phys Fluids.* 2003;15:1146–1157.
16. Achard JL, Cartellier A. Laminar dispersed two-phase flows at low concentration. I: Generalised system of equations. *Arch Mech.* 2000;52:25–53.
17. Achard JL, Cartellier A. Laminar dispersed two-phase flows at low concentration. II: Disturbance equations. *Arch Mech.* 2000;52:275–302.
18. Drew DA. Mathematical modeling of two-phase flow. *Ann Rev Fluid Mech.* 1983;50:133–166.
19. Joseph DD, Lundgren TS. Ensemble average and mixture theory equations for incompressible fluid-particle suspensions. *Int J Multiphase Flow*. 1990;16:35–42.
20. Cartellier A, Rivière N. Bubble-induced agitation and microstructure in uniforme bubbly flows at small to moderate particle Reynolds number. *Phys Fluids.* 2001;13:2165–2181.
21. Achard JL, Cartellier A. Laminar dispersed two-phase flows at low concentration. III: Pseudo-turbulence. *Arch Mech.* 2001;53:123–150.
22. Cartellier A. Screening mechanisms and induced agitation in bubbly flows at finite particle Reynolds numbers: experiments and preliminary modeling attempts using an hybrid approach. *Ercoftact Bull.* 2003;56.
23. Crispel S. *Modélisation statistique appliquée aux écoulements dispersés laminaires: mise en oeuvre et simulation.* Institut National Polytechnique de Grenoble, Grenoble, France; 2002, PhD thesis.
24. Tölke J, Krafcsyk M, Shulz M, Rank E. Lattice Boltzmann simulations of binary fluid flow through porous media. *Phil Trans R Soc Lond A.* 2002;360:535–545.
25. Rivière N, Cartellier A. Wall shear stress and void fraction in poiseuille bubbly flows: Part I and II. Simple analytic predictions. *Eur J of Mech B/Fluids.* 1999;18:823–867.
26. Crispel S, Cartellier A. Role of the Microstructure on the Bubble-

Induced Agitation: Recent Experiments and Simulations at Intermediate Particle Reynolds Numbers. Tsukuba, Japon; 2000.
27. Crispel S, Cartellier A, Simonin O, Achard JL. Laminar dispersed two-phase flow modeling applied to poiseuille bubbly flows. Aussois, France; 2000.
28. Legait B. Laminar flow of two phases through a capillary tube with variable square cross-section. *J of Colloïd and Interface Sci.* 1983;96: 28–38.
29. Taylor GI. Deposition of a viscous fluid on the wall of a tube. *J Fluid Mech.* 1960;10:161–165.
30. Nicklin DJ, Wilkes JO, Davidson JF. Two-phase flow in vertical tube. *Trans Instn Chem Engrs.* 1962;40:61–68.
31. Schwartz LW, Princen HM, Kiss AD. On the motion of bubbles in capillary tubes. *J Fluid Mech.* 1986;172:259.
32. Park CW, Maruvada SR, Yoon D. The influence of surfactant on the bubble motion in helle-shaw cells. *Phys Fluids.* 1994;10:3267–3275.
33. Ogawa K, Matsuka T, Hirai S, Okasaki K. Three-dimensional velocity measurement of complex Interstitial Flows through water-saturated porous media by tagging method in MRI technique. *Measurement Sci and Technol.* 2001;12:172–180.
34. Fairbrother F, Stubbs A. Studies in electroendosmosis. Part 6. The bubble-tube methods of measurement. *J Chem Sci.* 1987;1:527–529.
35. Taha T, Cui ZF. Hydodynamics of slug flow inside capillaries. *Chem Eng Sc.* 2004;59:1181–1190.
36. Colli Serano MT. *Hydrodynamique et transfert de chaleur dans un réacteur à lit fixe Gaz-Liquide-Solide.* Institut National Polytechnique de Lorraine, Nancy, France; 1993, PhD thesis.
37. Fabre J, Liné A. Modeling of two-phase slug flow. *Annual Rev Fluid Mech.* 1992;24:21–46.
38. Bretherton FP. The motion of long bubbles in tubes. *J Fluid Mech.* 1961;10:166–188.
39. Aussillous P, Quéré D. Quick deposition of a fluid on the wall of a tube. *Phys Fluids.* 2000;12:2367–2371.
40. Ratulowski J, Chang HC. Marangoni effects of trace impurities on the motion of long gas bubbles in capillaries. *J Fluid Mech.* 1990;210: 303–328.
41. Severino M, Giavedoni MD, Saita FA. A gas phase displacing a liquid with soluble surfactants out of a small conduit: the plane case. *Phys Fluids.* 2003;15:2961–2972.
42. Ratulowski J, Chang HC. Transport of gas bubbles in capillaries. *Phys Fluids A.* 1989;1:1642–1655.
43. Olbricht WL, Kung DM. The deformation and breakup of liquid drops in low Reynolds number flow through a capillary. *Physics of Fluids A.* 1992;4:1347–1354.
44. Cubaud T, Ho CM. Transport of bubbles in square microchannels. *Phys Fluids.* 2004;16:4575–4585.
45. Bordas ML. *Caractérisation des Ecoulements a bulles en lits fixes: expériences et modélisation.* Institut National Polytechnique de Grenoble/IFP-Solaize; 2002, PhD thesis.

Appendix: Derivation of the Mesoscale 1-D Model for a Bubbly Flow in a Fixed Bed

Local balance equations

- **liquid phase**

$$-\frac{\partial \alpha}{\partial t}+\frac{\partial}{\partial \mathbf{x}}\cdot[(1-\alpha)\mathbf{v}]=0 \tag{A1}$$

$$\rho_L D\mathbf{v}Dt=-\nabla p+\nabla\cdot\tau+\rho_L\mathbf{g}+\frac{1}{(1-\alpha)}[\nabla\cdot\pounds+\mathbf{M}-\rho_L\nabla\cdot A_{vv}] \tag{A2}$$

- **gas phase**

$$\frac{\partial \phi^{(1)}}{\partial t}+\frac{\partial}{\partial \mathbf{x}}\cdot\phi^{(1)}\mathbf{u}=0 \tag{A3}$$

$$\rho_G\frac{D\mathbf{u}}{Dt}+(1+R_1)[\nabla p-\nabla\cdot\tau]-\rho_G\mathbf{g}=-\frac{\rho_G}{\phi^{(1)}}\nabla\cdot A_{uu}+\frac{\mathbf{F}^*}{V_p} \tag{A4}$$

Definitions and assumptions

The spatial average $\langle f\rangle$ of a quantity f over the intersticial volume V_o trapped in the control volume is given by

$$\langle f\rangle=\frac{1}{V_o}\int_{V_o} f dx \tag{A5}$$

In the following, use will be also made of the surface average $\bar{f}$ evaluated over the fluid areas corresponding to the entrance S_{1F} or to the exit S_{2F} cross-sections of the control volume (Figure 3). If f is a scalar then

$$\bar{f}_i=\frac{1}{S_{iF}}\int_{S_{iF}} f dx \tag{A6}$$

and for a vector, denoting $\mathbf{n}_{iz}$ the external unit normal to the surface S_{iF} for $i=1$ or 2

$$\bar{f}=\frac{1}{S_{iF}}\int_{S_{iF}} \mathbf{f}\cdot\mathbf{n}_{iz} dx \tag{A7}$$

The following assumptions are made about the flow:

H1: The flow is stationary at mesoscale, that is: $(\partial\langle f\rangle/\partial t)=0$

H2: The phasic flows at mesoscale are unidirectional, and directed along z. Hence, the local phasic velocities are given by: $\mathbf{v}=\bar{V}\mathbf{n}_z+\mathbf{v}'$ for the liquid and $\mathbf{u}=\bar{U}\mathbf{n}_z+\mathbf{u}'$ for the gas where the unit vector $\mathbf{n}_z$ is directed along the z direction. Similarly, for the local gas fraction (and equivalently for the number density): $\alpha=\bar{\alpha}+\alpha'$. Consequently, one has: $\int_{S_{iF}}\mathbf{v}'\cdot\mathbf{n}_{iz}dx=0$ and $\int_{S_{iF}}\alpha' dx=0$ along the surfaces S_{1F} and S_{2F}.

H3: The phasic flows at mesoscale are fully developed. Thus, $(\partial\bar{f}/\partial z)=0$.

H4: When summing up flux terms involving fluctuations over two opposite lateral (that is, along x or y) faces of the control volume, the resulting contribution is assumed to be negligible, and it is canceled out.

H5: During the averaging process, terms appear that involve the cofluctuations of various quantities such as v'^2 or $\alpha' v'$. The surface integral of these terms are not strictly zero, but they are assumed to bring a negligible contribution, if any.

Spatial averaging of the liquid phase balances

Mass Balance. The time derivative commutes with the volume averaging operator. Thus, according to the assumption H1, all the time derivatives appearing in the balance equations disappear at mesoscale. The gradient term in Eq. A.1 is transformed using the Gauss theorem into a surface integral performed over the surface S_o bounding V_o. Let us introduce the unit normal $\mathbf{n}$ to the surface S_o: $\mathbf{n}$ is everywhere external to the fluid enclosed in the intersticial volume V_o. It is convenient to decompose the surface S_o, as the surface of the beads S_{obeads} inclosed (or partly enclosed) in the control volume plus the fluid area S_{ofluid} bounding that volume. S_{ofluid} comprises the cross-sections S_{1F} and S_{2F} plus the lateral fluid boundaries $S_{Flateral}$ with is the sum of the lateral fluid area S_{iF}, $i=x$ or

y bounding V_o (the later may enclose the outer wall depending on the selected control volume). Because of the stick condition that applies on the fixed solid matrix, the integration has only to be performed over the fluid area S_{ofluid} when the integrand involves a velocity. Going back to the gradient term in the continuity equation, and using the assumption H2, one has

$$\langle \partial(1-\alpha)\mathbf{v}/\partial\mathbf{x}\rangle = \frac{1}{V_o}\int_{S_o}(1-\alpha)\mathbf{v}\cdot\mathbf{n}d\mathbf{x} = \frac{1}{V_o}\left[\int_{S_{2F}}(1-\alpha) \times v_z d\mathbf{x} - \int_{S_{1F}}(1-\alpha)v_z d\mathbf{x} + \int_{SFlateral}(1-\alpha)v'\cdot\mathbf{n}d\mathbf{x}\right] = 0 \quad \text{(A8)}$$

The last integral disappears when using the assumptions H4 and H5. Hence, introducing the surface average of the liquid velocity and of the void fraction evaluated at the entrance and exit sections, the liquid mass conservation at mesoscale writes

$$\overline{V_2}(1-\overline{\alpha_2}) = \overline{V_1}(1-\overline{\alpha_1}) \quad \text{(A9)}$$

Thanks to the fully-developed assumption that holds for the liquid velocity as well as for the void fraction, that equality is automatically fulfilled. Note that, due to assumption H1, H3, and the fact that the porous medium in homogeneous, the surface average and the volume average are identical for the void fraction and for the phasic velocities.

Momentum equation

To produce a 1-D model, only the axial component of the momentum balance will be considered.

Convection term: The volume average of the convective term along the main flow direction z writes

$$\langle(\mathbf{v}\cdot\nabla\mathbf{v})\rangle_z = \frac{1}{V_o}\int_{V_o}(v_i\cdot\partial/\partial x_i)v_z d\mathbf{x} \quad \text{(A10)}$$

Using the decomposition of the velocity field (see H2), the main term is given by the volume integral of the quantity $\bar{V}d\bar{V}/dz$. According to the assumption H3, that contribution is zero. Hence, all the remaining contributions correspond to volume integral of quantities such as $v_i'\cdot\partial v_z/\partial x_i$. It is assumed that the fluctuating quantities involved in these products are sufficiently uncorrelated to cancel out after averaging over the control volume. Hence, no contribution remains from the convection term.

—**Stress in the liquid phase:** Let us first consider the pressure term. Its z-component is transformed as

$$\langle\nabla p\rangle_z = \frac{1}{V_0}\int_{S_o}(p\mathbf{n})_z d\mathbf{x} \quad \text{(A11)}$$

Contrary to velocity, the pressure does not vanish on the surface of the (fixed) solids. Using the decomposition of S_o as S_{obeads} plus S_{ofluid}, and neglecting a possible small contribution from pressure fluctuations

$$\langle\nabla p\rangle_z = \frac{1}{V_o}\int_{S_{ofluid}}(p\mathbf{n})_z d\mathbf{x} + \frac{1}{V_o}\int_{S_{obeads}}(p\mathbf{n})_z d\mathbf{x} = \frac{S}{V_o}(P_2-P_1) + \frac{1}{V_o}\int_{S_{obeads}}(p\mathbf{n})_z d\mathbf{x} \quad \text{(A12)}$$

The second integral in the r.h.s. contributes to the effort exerted on the beads. The axial viscous stress contribution is similarly transformed

$$\langle\nabla\cdot\tau\rangle_z = \frac{1}{V_o}\int_{S_o}(\tau\cdot\mathbf{n})_z d\mathbf{x} = \frac{1}{V_o}\int_{S_{obeads}}(\tau\cdot\mathbf{n})_z d\mathbf{x} + \frac{1}{V_o}\int_{S_{xF}\cup S_{yF}}(\tau\cdot\mathbf{n})_z d\mathbf{x} + \frac{1}{V_o}\int_{S_{1F}\cup S_{2F}}(\tau\cdot\mathbf{n})_z d\mathbf{x} \quad \text{(A13)}$$

The first integral contributes to the force exerted by the fluid on the solid matrix. The second integral corresponds to the viscous effort exerted on the lateral fluid areas bounding the control volume: it is noted $\tau_{lateral}S_{Flateral}/V_o$. When the control volume outer boundaries coincide with the walls of the vessel, this term represents the wall friction. It is then noted $\tau_{wall}S_{wall}/V_o$. The last integral, performed over the entrance S_{1F} and exit S_{2F} sections, involves only normal viscous stresses. Its neat contribution to the momentum balance writes

$$\frac{1}{V_o}\int_{S_{1F}\cup S_{2F}}(\tau\cdot\mathbf{n})_z d\mathbf{x} = \frac{1}{V_o}\left\{\int_{S_{2F}}(\tau_{zz}\cdot n_z)_2 d\mathbf{x} - \int_{S_{1F}}(\tau_{zz}\cdot n_z)_1 d\mathbf{x}\right\} = \frac{2\cdot\mu_L}{V_o}\left\{\int_{S_{2F}}\frac{\partial v_z}{\partial z}d\mathbf{x} - \int_{S_{1F}}\frac{\partial v_z}{\partial z}d\mathbf{x}\right\} \quad \text{(A14)}$$

Although such terms may not be zero because the flow is not fully-developed or steady at the microscale, the assumption H5 is expected to hold and the contribution of this term is neglected. Therefore

$$\langle\nabla\cdot\tau\rangle_z = \frac{1}{V_0}\int_{S_{obeads}}(\tau\cdot\mathbf{n})_z d\mathbf{x} + \tau_{lateral}\frac{S_{Flateral}}{V_o} \quad \text{(A15)}$$

—**Extra-deformation tensor:** The evaluation of the axial contribution of the extra-deformation tensor is similar to the transformation of the bulk viscous stress. The main difference is that, contrary to τ, the extradeformation tensor £ does not bring any contribution at the surface of the beads since perfect wetting has been assumed. Hence

$$\left\langle \frac{\nabla \cdot \pounds}{(1-\alpha)} \right\rangle_z = \frac{1}{V_o} \int_{S_o} \left(\frac{\pounds \cdot \mathbf{n}}{(1-\alpha)} \right)_z d\mathbf{x}$$

$$= \frac{1}{V_o} \int_{S_{Flateral}} \left\{ \frac{\alpha(\pounds_{zy} n_y + \pounds_{zx} n_x)}{1-\alpha} d\mathbf{x} \right\} \quad \text{(A16)}$$

since $\pounds \cdot \mathbf{n}_z = \pounds_{zz} n_z + \pounds_{zy} n_y + \pounds_{zx} n_x$. Thus, the only contribution left is due to the lateral fluid surfaces: it is noted $\pounds_{lateral} S_{Flateral}/V_o$. If the lateral boundaries of the control volume correspond to the duct walls, the above contribution disappears. Let us also recall that the contribution from the extradeformation tensor scales with the void fraction.

—**Turbulent and pseudo-turbulent stresses:** The tensor $\mathbf{A}_{vv}$ arises from liquid velocity fluctuations those origin is either due to an instability on the liquid phase (turbulence), or due to the agitation induced by the presence of bubbles. Its volume average is

$$\left\langle \frac{\nabla \cdot \mathbf{A}_{vv}}{1-\alpha} \right\rangle = \frac{1}{V_o} \int_{S_o} \frac{(\mathbf{A}_{vv}) \cdot \mathbf{n}}{1-\alpha} d\mathbf{x} = \frac{1}{V_o} \int_{S_{ofluid}} \frac{(\mathbf{A}_{vv}) \cdot \mathbf{n}}{1-\alpha} d\mathbf{x} \quad \text{(A17)}$$

since, by definition, this term is zero on solid surfaces. It is not prone to significantly contribute to the axial balance, owing to the strong viscous stress in the porous media considered here. In addition, and concerning the pseudo-turbulence, it has been shown[20] that for bubbly flows in large ducts, this term is insignificant for the momentum exchanges along the duct axis. The same conclusion certainly holds for a packed bed. Thus, no contribution of this tensor whatever its physical origin will be retained in the axial momentum balance.

—**Interfacial momentum source:** The expression of the interfacial momentum source can be simplified when there is scale separation between the bubble size and the characteristic dimension of the mean liquid velocity field. As no assumption is made here about these scales, the contribution of this term to the axial momentum balance, that is

$$\left\langle \frac{\mathbf{M}}{1-\alpha} \right\rangle_z = \left\langle \frac{M_z}{1-\alpha} \right\rangle = \frac{1}{V_0} \int_{V_0} \frac{M_z}{1-\alpha} d\mathbf{x} \quad \text{(A18)}$$

is not explicited further.

Mesoscale momentum balance for the liquid

The overall effort exerted by the liquid on the solid matrix enclosed in the control volume arises from the pressure and viscous stress contribution at the surface of the beads. Adding these two contributions allows us to introduce the liquid-solid force density f_{LS} defined as the force exerted by the liquid on the solid per unit volume of the intersticial fluid

$$f_{LS} = -\int_{S_{obeads}} (-p\mathbf{n} + \tau \cdot \mathbf{n})_z d\mathbf{x}/V_o \quad \text{(A19)}$$

the minus sign arising from the orientation of the normal. Collecting all the contributions and accounting for the thickness of the control volume $dz = V_o/S$ so that $(\bar{P}_2 - \bar{P}_1)(S/V_o) = d\bar{p}/dz$, the liquid momentum balance along the main flow direction z writes

$$-d\bar{p}/dz = \rho_L g + f_{LS} - (\tau_{lateral} + \pounds_{lateral}) S_{Flateral}/V_o - \langle M_z/(1-\alpha) \rangle \quad \text{(A20)}$$

If the lateral boundaries of the control volume are such as they correspond to the duct wall, the contribution $\pounds_{lateral}$ of the extra-deformation tensor disappears (there are no interfaces on the vessel walls), and the remaining term $\tau_{lateral}$ corresponds to the wall friction τ_{wall}. Introducing the force density $f_{Lwall} = -\tau_{wall} S_{wall}/V_o$ corresponding to the stress exerted by the fluid on the wall, the 1-D momentum balance written for the entire cross-section of the three-phase system reads

$$-\frac{d\bar{p}}{dz} = \rho_L g + f_{LS} + f_{Lwall} - \langle M_z/(1-\alpha) \rangle \quad \text{(A21)}$$

This equation applies to any orientation of the flow with respect to gravity provided that the axis z is directed along the main flow and that g is understood as:

$$g = -|g| cos(\mathbf{n}_z, \mathbf{g}) \quad \text{(A22)}$$

With such conventions, all the quantities $-(d\bar{p}/dz)$, f_{LS}, and f_{Lwall} are positive.

Spatial averaging of the dispersed phase balances

Continuity. Following the same developments as for the liquid continuity equation, the mass conservation for the gas phase leads to

$$\bar{U}_2 \bar{\alpha}_2 = \bar{U}_1 \bar{\alpha}_1 \quad \text{(A23)}$$

Again, assuming a fully developed flow at mesoscale implies that the above equation is automatically satisfied. Again, one has $\bar{U} = \langle U \rangle$.

Momentum. Starting from the momentum Eq. A4 written for massless bubbles, its righthand side term integrated over the control volume provides $\langle (F^*/V_p) \rangle$ that represents the average force density acting on a test bubble. The averaging of the term $\nabla p - \nabla \cdot \tau$ has already been done. The term involving the operator R_1 is kept as it is. Thus

$$\frac{d\bar{p}}{dz} + \langle R_1[\nabla p - \nabla \cdot \tau] \rangle_z + f_{LS} - \tau_{lateral} S_{Flateral}/V_o = \langle (F_z^*/V_p) \rangle \quad \text{(A24)}$$

and for a control volume extending to the walls of the vessel

$$\frac{d\bar{p}}{dz} + \langle R_1[\nabla p - \nabla \cdot \tau] \rangle_z + f_{LS} + f_{Lwall} = \langle (F_z^*/V_p) \rangle \quad \text{(A25)}$$

Final set of equations

For a control volume enclosed in the porous medium, the extra viscous stress $\mathfrak{L}_{lateral}$ due to the presence of liquid-gas interfaces can be considered as negligible compared with the viscous stress exerted on the solid boundaries (let us also recall that $\mathfrak{L}_{lateral}$ is $O(\alpha)$). The viscous stress on the lateral fluid surfaces of the control volume can be similarly neglected. For a control volume extending up to the vessel walls, $\tau_{lateral}$ can be neglected compared with the stress on the solid matrix f_{LS} provided that the column is large enough (alternately, the contribution $\tau_{lateral}$ could be included in f_{LS}).

In both cases, the momentum equations can be simplified into

$$-\frac{d\bar{p}}{dz} = \rho_L g + f_{LS} - \langle M_z/(1-\alpha)\rangle \tag{A26}$$

$$-d\bar{p}/dz = f_{LS} + \langle R_1[\nabla p - \nabla\cdot\tau]\rangle - \langle F_z^*/V_p\rangle \tag{A27}$$

For very small bubbles, one has: $M_z = -\alpha F_z^*/V_p$. Also, the contributions from the flow inhomogeneities related with the operator R_1 become negligible. Let us introduce the momentum exchange from the liquid to the gas f_{LG} as equal to the following force density

$$f_{LG} = \left\langle \frac{\alpha}{(1-\alpha)} F_z^*/V_p \right\rangle = \frac{\bar{\alpha}}{(1-\bar{\alpha})} \langle F_z^*/V_p\rangle \tag{A28}$$

where the last equality is expected to hold in homogeneous conditions. Note that f_{LG} as defined above equals $1/(1-\alpha)$ times the f_{LG} introduced by Attou and Ferschneider. Thus, one has

$$-\frac{d\bar{p}}{dz} = \rho_L g + f_{LS} + f_{LG} \tag{A29}$$

$$-d\bar{p}/dz = f_{LS} - \frac{(1-\bar{\alpha})}{\bar{\alpha}} f_{LG} \tag{A30}$$

which can be rewritten

$$-\frac{d\bar{p}}{dz} = (1-\bar{\alpha})\rho_L g + f_{LS} \tag{A31}$$

$$f_{LG} = -\bar{\alpha}\rho_L g \tag{A32}$$

These equations are valid whatever the flow orientation when using the conventions mentioned earlier.

Manuscript received Feb. 24, 2006, and revision received Jun. 19, 2006.